Received: 2 October 2019 | Revised: 26 January 2020 | Accepted: 23 February 2020

DOI: 10.1002/nme.6345

RESEARCH ARTICLE

WILEY

A hybrid material-point spheropolygon-element method for solid and granular material interaction

Yupeng Jiang[1,2] | **Minchen Li**[2] | **Chenfanfu Jiang**[2] | **Fernando Alonso-Marroquin**[1]

[1]School of Civil Engineering, The University of Sydney, Sydney, New South Wales,Australia

[2]Department of Computer and Information Science, University of Pennsylvania, Philadelphia, Pennsylvania,USA

Correspondence
Yupeng Jiang, School of Civil Engineering, The University of Sydney, Sydney, NSW, Australia.
Email: yupeng.jiang@sydney.edu.au

Funding information
Australia research council, Grant/Award Number: LP160100280

Summary

Capturing the interaction between objects that have an extreme difference in Young's modulus or geometrical scale is a highly challenging topic for numerical simulation. One of the fundamental questions is how to build an accurate multiscale method with optimal computational efficiency. In this work, we develop a material-point-spheropolygon discrete element method (MPM-SDEM). Our approach fully couples the material point method (MPM) and the spheropolygon discrete element method (SDEM) through the exchange of contact force information. It combines the advantage of MPM for accurately simulating elastoplastic continuum materials and the high efficiency of DEM for calculating the Newtonian dynamics of discrete near-rigid objects. The MPM-SDEM framework is demonstrated with an explicit time integration scheme. Its accuracy and efficiency are further analyzed against the analytical and experimental data. Results demonstrate this method could accurately capture the contact force and momentum exchange between materials while maintaining favorable computational stability and efficiency. Our framework exhibits great potential in the analysis of multi-scale, multi-physics phenomena.

KEYWORDS

coupling algorithm, granular mechanics, material point method, multibody numerical simulation, spheropolygon discrete element method

1 | INTRODUCTION

The numerical simulation of the multibody system is crucial for understanding several key issues in geomechanics, such as the mechanical properties of the complex granular matrix,[1-3] the interaction between the debris flow and solid structures.[4-6] It could also benefit the physics-based simulation in computer graphics (CG) to generate photorealistic visual effects for solid-fluid (or granular media) animation.[7,8] These systems commonly consist of individual bodies with disproportional sizes and various shapes. The fines-ballast granular structure typically exists at the railroad foundation,[9] where the ratio between the volume of small (fines) and big particles (ballast) reaches a level of 1:10.[5] Components in the system could have distinctively different Young's modulus. For example, the crumb rubbers are artificially added to the railroad or highway foundation for preventing the breakage of surrounding granite particles and further improving the stability.[10] It is also common in CG production to animate intricate multibody frictional contact between soft and rigid objects. The numerical methods for these issues often require an accurate simulation for the deformation of the individual bodies and contact forces among them. In other words, both the elastodynamic and the kinetic behaviors of each

body need to be properly calculated. The finite-element method (FEM) is commonly applied, and proper treatment of the spatial discretization is essential for each component of the system.[11,12] However, the accuracy and stability of FEM suffer from the potentially strong distortion of the meshes. Such a problem can be alleviated only by remeshing schemes,[13] which, on the other hand, highly compromises the computational efficiency. The material point method (MPM) offers an attractive alternative approach. It discretizes the computational domain with meshless particles and therefore avoids the difficulties encountered during large mesh deformation or topology changes. Because the deformation history of the material domain is stored and represented by material points, MPM utilizes a fixed Eulerian background grid that is not distorted during the simulation. MPM and its variants have been successfully applied for the study of continuum granular materials,[14] crack propagation in snow,[15] and computer animation.[16]

As a numerical method based on continuum mechanics, either FEM or MPM requires a spatial discretization for every part of a multibody system. Even for many engineering applications where only the kinematic information of near-rigid bodies is focused, the calculation of continuum partial differential equations (PDEs) still needs to be performed upon them.[11] The high stiffness of the material requires extremely small time-step intervals for the stability of the simulation, while the convergence of iterative solvers in the implicit scheme is slow. Meanwhile, both methods use relatively complicated ways to handle the collision and contact force.[17-19] One of the inspiring ideas was proposed by Guilkey et al,[20] which states each material should be described and evolves in its preferred reference frame. In our case, the computational efficiency could be largely improved if the near-rigid components are properly simplified so that only an accurate description of kinetic information is provided. The discrete element method[21] (DEM) has high efficiency for simulating the Newtonian movements of rigid bodies. It treats near-rigid bodies, or particles, as perfectly rigid and defines an interaction zone that is coated outside each of them using neighbor detection algorithms. The contact forces are calculated based on the depth, area, or volume of the intersections among particle zones. This reasonable simplification ignores the deformation for the particles while accurately simulates the momentum and contact forces through contact laws. No spatial discretization or mesh generation is involved.

The coupling between DEM and other numerical methods (FEM, MPM) potentially provides an optimized balance between computational time and accuracy. Several methods have been systematically developed. For example, the DEM-FEM approach is conducted for hierarchical multiscale modeling of granular media and the interaction between the tire tread and granular terrain.[22] The DEM is coupled with the lattice Boltzmann method (LBM) and computational fluid dynamics to study the interaction between the fluid and particulate system.[23,24] The results of these simulations well agree with experimental data and analytical solutions. But neither of these methods can be used to model the interaction between the rigid body and granular materials that has elastic shear resistance such as powders and fines.

One of the recent milestones for the coupling of MPM and DEM was conducted by Liu et al.[25] The authors modeled a 2D sand pile collapsing and impacting three rectangular wooden blocks. The granular flow is simulated with MPM. A shrunken-point DEM is used to calculate the movement of blocks. Nine material points are attached at the corners, center of the edges, and the geometrical center of each block. The contact between DEM blocks and the MPM flow is detected through the mutual background grid node. Contact forces are calculated at the mutual projection gird based on the momentum information and applied to geometrical nodes on the DEM parts as body forces. The numerical results show a reasonable agreement with the experimental data. This method could further help the damage analysis of buildings under the impact of debris flow. An MPM-DEM[26] hybrid method also developed to exploits the dual strengths of discrete and continuum treatments. However, this method is mainly focused on the improvement of the efficiency of DEM for simulating the granular flow. Discrete elements and material points are replacing each other under certain criteria rather than coexisting and interacting.

Liu et al's method[25] unifies the coupling procedures under the computational frame of MPM. It inevitably inherits an issue of MPM for handling the contacts, which is the strong dependency of the background grid system. First, the collision handling in MPM is calculated based on the proportions of momentum that different objects mutually contribute to grids. Contact detection and the calculation of force are fundamentally affected by the resolution and the structure of the grid system. Second, the contact algorithm needs to separately calculate the momentum for each object. The simulation will be computationally expensive if it involves a large number of discrete bodies. Meanwhile, the influence of shape is also omitted by simplifying the DEM particles with few material points. For many cases, such simplification is non-trivial and not rigorously discussed. The accuracy of the angular momentum of DEM particles is highly compromised since the forces are only applied at the geometrical nodes. These problems limit the performance of the coupling method and diminish the advantage of using DEM as a rigid body simulator. Therefore, we believe it is necessary to develop an advanced numerical method that could mitigate these issues and provide a more general way for the coupling between DEM and MPM.

In this article, we develop a different coupling method between the DEM and MPM. The rigid body is represented by spheropolygon DEM (SDEM).[27] It was developed for simulating the movement of irregular discrete particles. Comparing with other DEM-based methods, the SDEM could efficiently handle the contact forces among irregular particles and preserve the conservation of mechanical energy. Due to these merits, SDEM has been coupled with the boundary element method for simulating subparticle stress and particle breakage.[28] The interactions between the fluid and irregular rigid bodies are also studied using the LBM-SDEM.[29] In this work, the MPM is used for simulating the deformable part of the multibody system. Two different constitutive models, linear elasticity and elastoplastic Drucker-Prager model, are used to study the elastic-rigid and granular-rigid coupling, respectively. The contact between SDEM and MPM is detected with the Euclidean distance instead of the existence of mutual projection grids. Coupling forces are directly calculated with a well-established DEM contact model. For rigid particles, forces are applied at the exact contact position. In summary, our method unifies the coupling procedure under the computational frame of DEM. It significantly reduces the coupling dependency to the MPM background grid. The contact detection and force calculation only happen at the boundary of the rigid particles, which are more efficient than that of the pure MPM. The influence of particle shape can be better preserved and no longer needs to be simplified with material points.

This article is organized as follows. The computational methodology for MPM and SDEM is introduced in Sections 2 and 3, respectively. The coupling method is presented in Section 4. A serial of numerical tests is conducted in Sections 5 and 6. Results are rigorously discussed with analytical solutions and experimental data as verification and validations for the MPM-SDEM. Potential applications of this method are provided in Section 7. General conclusions are presented in Section 8.

2 | MPM FOR ELASTIC AND GRANULAR MATERIAL

The MPM is a hybrid scheme utilizing both Lagrangian particles and Eulerian grids.[30,31] It follows the governing equations of the continuum mechanics and its discretization is derived from the Galerkin weak form of momentum conservation, similar to the FEM. However, unlike the FEM, which discretizes the computational area into piecewise subdomains on a mesh, the MPM uses the particlewise material regions to represent the continuum. Lagrangian variables such as mass, momentum, and position are carried by the material points. The embedding relationship between Eulerian grids and material points is commonly defined by the nodal shape functions. At each time step, Lagrangian variables carried by material points need to be first transferred to the corresponding grid nodes. The equation of motion is solved at the grid nodes, while volume integrals are approximated through particle quadrature, and the velocity is updated accordingly and then interpolated back to material points for their advection and strain updates. Eulerian grids are restored to a standard Cartesian configuration after each time step, and only the values and derivatives of the nodal shape functions are constantly recalculated at the beginning of the next time step.

2.1 | Governing equations and discretization for MPM

The Lagrangian kinematic description of a continuum body needs to satisfy a group of PDEs, including conservation of mass, momentum, and energy. These PDEs are known as governing equations, which, combined with the material constitutive model and boundary conditions, determine the behavior of the material. The conservation of mass is inherently satisfied in MPM since the material points in this study are assigned with constant mass values. The conservation of energy is guaranteed because the simulation assumes an isothermal setting that does not involve the exchange of heat. Therefore, the dynamic state of the material can be obtained by solving the conservation of moment[20,25,32]:

$$\sigma_{ij,j} + \rho b_i = \rho \ddot{u}_i, \tag{1}$$

where ρ is the density of the material; u_i denotes the displacement, the dots are the notation for the order of time derivative; σ_{ij} is the Cauchy stress tensor, the subscript denotes the components and the deviator of the tensor; b_i is the body force term. The PDEs follow Einstein notation. Equation 1 can be solved in the domain Ω through its weak form:

$$\int_\Omega u_i^* (\sigma_{ij,j} + \rho b_i - \rho \ddot{u}_i) d\Omega = 0, \tag{2}$$

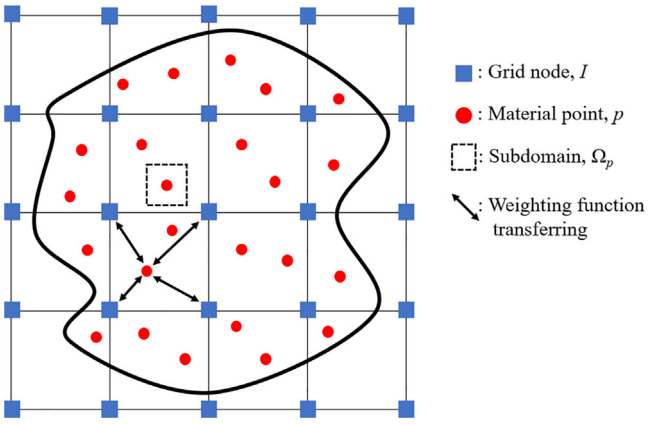

FIGURE 1 Discretization schemes for the material point method [Color figure can be viewed at wileyonlinelibrary.com]

and boundary conditions:

$$\mathbf{t}(\mathbf{x})|_{\Gamma_t} = \mathbf{t}_0, \mathbf{u}(\mathbf{x})|_{\Gamma_u} = \mathbf{u}_0, \tag{3}$$

where the computational domain is denoted as Ω; $\mathbf{u}^*$ represents the virtual displacement which equals zero on the boundary section Γ_u; the value of traction $\bar{t}_i$ is known at the boundary Γ_t. Combining the boundary conditions, Equation 3 can be further written as:

$$\int_\Omega \rho \ddot{u}_i u_i^* d\Omega + \int_\Omega \sigma_{ij,j} u_i^* d\Omega - \int_\Omega \rho b_i u_i^* d\Omega - \int_{\partial\Omega} t_i u_i^* d\Gamma. \tag{4}$$

As shown in Figure 1, the domain is discretized by the material points (red dots), here also called "Lagrangian Points." The information of deformation gradient, mass, and momentum is carried by these Lagrangian points. Eulerian background grid nodes (blue squares) are defined as background scratchpad. At each time step, the variables are first interpolated to grid nodes using multidimensional shape functions. The information is then updated at grid nodes and transferred back to the material points for the next time step. The perspective of the generalized interpolation MPM (GIMP) is adopted for the discretization[32,33] process of the governing equation (Equation 4). Each material point occupies a partition Ω_p in the entity Ω:

$$V_p = \int_{\Omega_p \cap \Omega} \chi_p(\mathbf{x}) d\Omega, \tag{5}$$

where V_p is the initial volume and $\chi_p(\mathbf{x})$ is the characteristic function, the subscript p denotes the value on the material point. The mass of the material m_p can be written as:

$$m_p = \int_{\Omega_p \cap \Omega} \rho_p(\mathbf{x}) \chi_p(\mathbf{x}) d\Omega, \tag{6}$$

where $\rho_p = m_p / V_p$ is the density of the material. There are mainly two different forms of $\chi_p(\mathbf{x})$. One is using the total discrete approach (DMPM):

$$\chi_p(\mathbf{x}) = \delta(\mathbf{x} - \mathbf{x}_p) V_p, \tag{7}$$

where $\mathbf{x}_p$ is the spatial coordinate of the material point and δ is the Dirac delta function. The mass only exits at the discrete position over the entire computational domain. The other method is to use GIMP, where the form of $\chi_p(\mathbf{x})$ for each material points to be a continuous function (constant, linear, or even a higher-order) over the Ω_p. A given physical variable k in the computational domain can be approximated by the value k_p carried by the relevant material points and their characteristic functions:

$$k(\mathbf{x}) = \sum_p k_p \chi_p(\mathbf{x}). \tag{8}$$

Equation (4) can be converted from the continuous integration form into a summation of material points:

$$\sum_p \int_{\Omega_p \cap \Omega} \frac{\dot{p}_{ip}}{V_p} \chi_p u^*_{ip} d\Omega = -\sum_p \int_{\Omega_p \cap \Omega} \sigma_{ijp} \chi_p u^*_{ip,j} d\Omega + \sum_p \int_{\Omega_p \cap \Omega} \frac{m_p}{V_p} \chi_p b_{ip} u^*_{ip} d\Omega + \int_{\partial\Omega} t_{ip} u^*_{ip} d\Gamma. \tag{9}$$

The behaviors of the continuous material are now defined by the physical variables carried by material points. Equation 9 needs to be solved on the background grid nodes. The relation of virtual displacement between the grid node and material points is written as:

$$\mathbf{u}^*_p = \sum_I N_{Ip}(\mathbf{x}_p)\mathbf{u}^*_I, \quad \mathbf{u}^*_{p,j} = \sum_I N_{Ip,j}(\mathbf{x}_p)\mathbf{u}^*_I. \tag{10}$$

The subscript I is the indexes that denote a value is on the grid node I. Substituting Equation 10 into Equation 9 to eliminate the virtual displacement, the equation of motion can be rewritten as:

$$\dot{\mathbf{p}}_I = \mathbf{f}^{\text{int}}_I + \mathbf{f}^{\text{ext}}_I, \quad \mathbf{x}_I \notin \Gamma_u, \tag{11}$$

where $\mathbf{p}_I$ is the momentum for the grid node; $\mathbf{f}^{\text{int}}_I + \mathbf{f}^{\text{ext}}_I$ represent the internal and external force applied on the grid node, respectively:

$$\dot{p}_{iI} = \sum_p \dot{p}_{ip} S_{Ip} \tag{12}$$

$$f^{\text{int}}_{iI} = -\sum_p \sigma_{ijp} S_{Ip,j} V_p \tag{13}$$

$$f^{\text{ext}}_{iI} = \sum_p m_p b_{ip} S_{Ip} + \int_{\partial\Omega} t_i N_{Ip} d\Gamma. \tag{14}$$

The interpolation of variables between the material points and the grid nodes is calculated using the weighting function $S_{Ip}(\mathbf{x})$:

$$S_{Ip}(\mathbf{x}) = \frac{1}{V_p} \int_{\Omega_p \cap \Omega} \chi_p(\mathbf{x}) N_{Ip}(\mathbf{x}) d\Omega \tag{15}$$

$$S_{Ip,j}(\mathbf{x}_p) = \frac{1}{V_p} \int_{\Omega_p \cap \Omega} \chi_p(\mathbf{x}) N_{Ip,j}(\mathbf{x}) d\Omega. \tag{16}$$

This interpolation is often referred to as *P-G* (particle to grid) transferring and the reverse process is *G-P* (grid to particle) transferring. The specific forms of $S_{Ip}(\mathbf{x})$ depend on the choice of interpolation method (DMPM or GIMP) and shape function, which is provided in the Appendix. The interpolation function in GIMP has C^1 continuity even if the shape function is only a linear function with C^0 continuity. Generally, GIMP is more stable for spatial discretization, and it produces less computational noises when the material points moving from one grid cell to another (cell-crossing noise). However, DMPM with quadratic or cubic B-spline weighting functions also has its advantage for being able to use a noise-free and angular momentum conserving transferring scheme called affine-particle-in-cell method (APIC).[34] Note that as pointed out by Gao et al,[7] that GIMP and quadratic-B-Spline-DMPM are equivalent when particle domain is chosen to be a box with its width equal to the grid cell spacing.

2.2 | Time integration scheme

The computational domain is time-variant, which indicates that Equation 11 needs to be fulfilled at each time step. The central difference method is applied for the update of the grids' momentum:

$$\mathbf{p}^{n+1/2}_I = \mathbf{p}^{n-1/2}_I + \mathbf{f}^n_I \Delta t, \tag{17}$$

where superscript n denotes the sequence of the time step and Δt is a constant interval of the time increment at each step; $\mathbf{f}_I^n$ equals $\mathbf{f}_I^{\text{ext}}+\mathbf{f}_I^{\text{int}}$ is the total nodal force. In this article, we use the update-stress-first (USF)[35] format for the optimal efficiency and the conservation of energy of the simulation. The USF format general has a minimal dissipation for energy but less stable than the update-stress-last (USL) format, especially for simulating the osculation with unresolved mode.[35] It is a more suitable format for examining the energy conservation of the coupling method.

The algorithm to update the nodal and point variables is introduced in its computational sequences:

1. The nodal mass m_I, momentum $\mathbf{p}_I$, and velocity $\mathbf{v}_I$ are calculated through the interpolation of the corresponding material points and their weighting function S_{Ip}:

$$m_I^n = \sum_p m_p S_{Ip}^n, \tag{18}$$

$$\mathbf{p}_I^{n-1/2} = \sum_p m_p \mathbf{v}_p^{n-1/2} S_{Ip}^n, \tag{19}$$

$$\mathbf{v}_I^{n-1/2} = \mathbf{p}_I^{n-1/2} / m_I^n. \tag{20}$$

2. The material point's strain $\dot{\varepsilon}_{ijp}^{n-1/2}$ and spin $\dot{\Psi}_{ijp}^{n-1/2}$ rate tensors are obtained with the nodal velocities[24]:

$$\dot{\varepsilon}_{ijp}^{n-1/2} = \frac{1}{2}\sum_I (S_{Ip,j}^n v_{iI}^{n-1/2} + S_{Ip,i}^n v_{jI}^{n-1/2}), \tag{21}$$

$$\dot{\psi}_{ijp}^{n-1/2} = \frac{1}{2}\sum_I (S_{Ip,j}^n v_{iI}^{n-1/2} - S_{Ip,i}^n v_{jI}^{n-1/2}), \tag{22}$$

where the value of S_{Ip} is decided according to the method of spatial discretization and the relative position between the material point and grid node. The strain and stress are then calculated as:

$$\varepsilon_{ijp}^n = \varepsilon_{ijp}^{n-1} + \dot{\varepsilon}_{ijp}^{n-1/2}\Delta t, \tag{23}$$

$$\sigma_{ijp}^n = \sigma_{ijp}^{n-1} + \dot{\sigma}_{ijp}^{n-1/2}\Delta t. \tag{24}$$

The stress rate is determined by:

$$\dot{\sigma}_{ij} = \overset{\nabla}{\sigma}_{ij} + \sigma_{ik}\psi_{jk} + \sigma_{jk}\psi_{ik}, \quad \overset{\nabla}{\sigma}_{ij} = C_{ijkl}\dot{\varepsilon}_{kl}, \tag{25}$$

where Jaumann stress rate $\overset{\nabla}{\sigma}_{ij}$ for linear elasticity is adopted to eliminate the influence of pure rotation to the Cauchy stress tensor. The specific form of stress rate $\dot{\sigma}_{ij}$ depends on the constitutive model.

3. The internal and external nodal forces are updated using the material point's stress, the body force term $\mathbf{b}_p$, and the boundary traction $\mathbf{t}_p$ according to Equations 12 and 13
4. Equation 11 is solved at the grid nodes with the nodal forces and momentum to further update the velocity and position of material points. There are three methods for this specific G-P transferring procedure, particle-in-cell format (PIC),[30,36] fluid-implicit-particle format (FLIP),[37] and the hybrid format. The PIC transferring update the material's velocity directly using the interpolation functions and corresponding grid values:

$$\mathbf{v}_p^{n+1/2} = \sum_I \mathbf{p}_I^{n+1/2} S_{Ip}^n / m_I^n. \tag{26}$$

This transferring method has a strong numerical dissipation; the angular momentum and kinetic energy of material points decrease rapidly with the progress of iterations. This problem makes the PIC format unsuitable for simulating

dynamic problems such as the landslide. Because the kinetic energy of granular flows is not accurate enough and hence makes the results unreliable. However, this dissipation effect is not entirely undesirable. It efficiently decreases the vibration in quasistatic simulations, which generated by the initial configuration of the objects, and helps the system to reach an equilibrium. The FLIP updates the velocity using the nodal force:

$$\mathbf{v}_p^{n+1/2} = \mathbf{v}_p^{n-1/2} + \Delta t \sum_I \mathbf{f}_I^n S_{Ip}^n / m_I^n. \tag{27}$$

It greatly improves the conservation of angular momentum. But the exact conservation can only be achieved by using the "full" mass matrix instead of lumped mass matrix, which is necessary for the numerical stability but impractical due to its potential singularity.[34,38] Meanwhile, FLIP format generates the so-called "ringing instability" because of noisy velocity modes in the null space of the transfer operator. It causes the numerical instability when simulating the granular material with strong dynamic behaviors. A better way to preserve the advantages of PIC and FLIP is to use a hybrid transferring format[39]:

$$\mathbf{v}_p^{n+1/2} = \alpha \sum_I \mathbf{p}_I^{n+1/2} S_{Ip}^n / m_I^n + (1-\alpha)\left(\mathbf{v}_p^{n-1/2} + \Delta t \sum_I \mathbf{f}_I^n S_{Ip}^n / m_I^n\right), \tag{28}$$

where α is the coefficient that ranges between 0 and 1; $\alpha = 0$ is the pure FLIP format and $\alpha = 0$ gives the pure PIC format. The value of α is proportional to the magnitude of the dissipation effect and can be used for controlling the damping for the quasi-static simulation. The instability of the FLIP format is also alleviated. However, the hybrid method still has an issue. No rigorous analysis to define the quantitative relation between the dissipation and the value of α. The behavior of the material is also sensitive to the variation of α and the numerical damping highly depends on the time step size. Especially for the granular material, the specific value of the coefficient is rather an empirical setting.

Such a problem can be properly solved by using APIC format or extended-particle-in-cell format (XPIC).[40] We adopt APIC in this article. This innovative method is developed by Jiang and Schroeder.[34] It represents particle velocities as locally affine, which allows APIC to conserve linear and angular momentum across transfers. This transferring format effectively reduces the numerical dissipation; it also does not experience the velocity noise and instability in FLIP. It has been applied for the simulation of both the granular and hyperelastic material and exhibits superior performance. The APIC still uses the PIC format for the velocity and position update of material points at step (**d**). However, APIC applies a different scheme for the *P-G* transferring procedure at step (**a**), which is written as[34,41]:

$$\mathbf{D}_p^n = \sum_I N_{Ip}^n (\mathbf{x}_I^n - \mathbf{x}_p^n)(\mathbf{x}_I^n - \mathbf{x}_p^n)^T = \begin{cases} L^3\mathbf{I}/3 & \text{cubic} \\ L^2\mathbf{I}/4 & \text{quadratic} \end{cases}, \tag{29}$$

$$\mathbf{p}_I^{n-1/2} = \sum_p m_p N_{Ip}^n (\mathbf{v}_p^{n-1/2} + \mathbf{B}_p^n (\mathbf{D}_p^n)^{-1} (\mathbf{x}_I^n - \mathbf{x}_p^n)), \tag{30}$$

where L is the grid spacing and $\mathbf{I}$ is the unit matrix; the additional matrix $\mathbf{D}_p$ serves as the inertia matrix for affine motion and $\mathbf{B}_p$ contains the angular momentum information and updates as:

$$\mathbf{B}_p^{n+1/2} = \sum_I S_{Ip} v_I^{n+1/2} (\mathbf{x}_I^n - \mathbf{x}_p^n)^T. \tag{31}$$

In this article, we use the GIMP with the hybrid format for simulating the linear elastic material and DMPM with APIC format for the granular material. The quadratic kernel is adopted as the shape function.

2.3 | Constitutive models

The physical properties of granular material have been a difficulty for the numerical simulation. Large deformation may happen due to the elastoplastic behavior of granular material, which causes trouble for the mesh-based method. The MPM, therefore, has a unique advantage for simulating both quasistatic deformation and granular flow without the

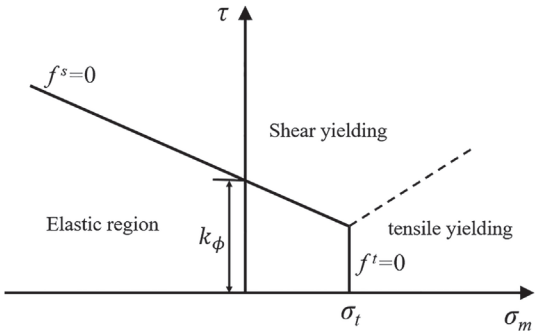

FIGURE 2 Yield criteria of Drucker-Prager (D-P) model that includes the tensile stress cut-off[24]

restriction of mesh. The Drucker-Prager plasticity model (*D-P*) is employed to simulate the granular material. This model has been widely applied for the engineering application and MPM sand simulation. Although the Jaumann stress rate introduced earlier may not be exceedingly accurate for moderate deformation with deviatoric strains that more than 10% (eg, granular flow),[42] it can still provide reasonable results and we choose to use it for a direct comparison to the results in the existing literature.[25]

The yield criteria in *D-P* model are shown in Figure 2 and defined as:

$$f^s = \tau + q_\phi - k_\phi, \tag{31}$$

$$f^t = \sigma_m - \sigma^t, \tag{32}$$

where f is the yielding surface, the superscripts s and t denote the shear and tensile yielding behavior respectively; σ^t is the tensile strength; τ is the equivalent shear stress and σ_m is the spherical stress:

$$\tau = \sqrt{J_2}, J_2 = s_{ij}s_{ij}/2, \tag{33}$$

$$\sigma_m = I_1/3, \quad I_1 = \sigma_{kk}, \tag{34}$$

where J_2 is the second invariant of the deviatoric stress tensor and s_{ij} is the deviatoric stress components; I_1 denotes the first invariant of the stress tensor. The coefficients q_ϕ and k_ϕ are the frictional coefficient and yield stress for shearing behavior, respectively. They are calculated based on the friction angle ϕ and the cohesion term c:

$$q_\phi = \frac{3\tan\phi}{\sqrt{9 + 12\tan^2\phi}}, \quad k_\phi = \frac{3c}{\sqrt{9 + 12\tan^2\phi}}. \tag{35}$$

MPM uses the return mapping[24] method to detect whether the yielding conditions are fulfilled at each time step. The isotropic linear elasticity is used for solid material:

$$C_{ijkl} = K\delta_{ij}\delta_{kl} + G\left(\delta_{ik}\delta_{jl} + \delta_{il}\delta_{jk} - \frac{1}{3}\delta_{ij}\delta_{kl}\right), \tag{36}$$

where $\mathbf{C}$ is the constitutive tensor; K and G are the bulk and shear module, respectively.

3 | SPHEROPOLYGON DISCRETE ELEMENT METHOD

The SDEM[27] is selected as the DEM part of the hybrid algorithm due to its unique advantages. The geometrical irregularity of a particle is properly represented as a Minkowski sum of a polygon with a disk, and the multiple contacts between irregular particles are calculated based on distances between vertices and edges. These features make it computationally efficient.[25] The contact information between MPM and the SDEM can be easily applied to the correct position of SDEM instead of its geometrical modes. The point contact relation is also more realistic for contacts between rigid bodies and granular materials.

FIGURE 3 Spheropolygon element obtained by sweeping a disk around a polygon [Color figure can be viewed at wileyonlinelibrary.com]

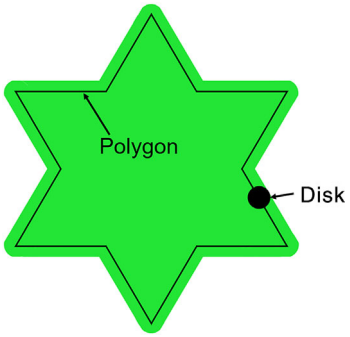

3.1 | SDEM algorithm

A spheropolygon is the Minkowski sum of a polygon to represent the irregular shape of a near-rigid object and a disk with radius a, which defines an elastic area to calculate the contact forces that generated among particles. Mathematically the Minkowski sum of two sets of points P and Q of a vector space is given by[27]:

$$P + Q = \{\mathbf{x} + \mathbf{y} | \ \mathbf{x} \in P, \mathbf{y} \in Q\}. \tag{37}$$

The geometrical interpretation of this operation is equivalent to the sweeping of a disk around the profile of the polygon while maintaining its original orientation. For example, the DEM particle with a shape of the hexagram in Figure 3 is properly approximated by a spheropolygon element with a few boundary lines and a disk sweeping its profile. The hexagram defines the element shape, and the disk is used for contact force calculation. SDEM has been proved as a more effective approach than using a cluster of small particles to approach this shape, especially when the particle shape is more irregular or complicated.

The contact force of the spheropolygon is defined through a vertex-edge contact relationship. Let us consider two spheropolygons SP_i and SP_j with their polygons P_i and P_j and the radii of the disks a_i and a_j. Each polygon is defined by its own set of vertices $\{V\}$ and edges $\{E\}$. The overlapping length ξ between each vertex-edge pair (V, E) is written as:

$$\xi(V, E) = \langle a_i + a_j - d(V, E) \rangle, \tag{38}$$

where $d(V, E)$ is the Euclidean distance between the vertex V and the edge E. The brace at the right side of the equation means the nonnegative limit of ξ. Therefore, the force vector $\mathbf{F}$ applied on particle i by particle j is expressed as:

$$\mathbf{F}_{ij} = -\mathbf{F}_{ji} = \sum_{V_i E_j} \mathbf{F}(V_i, E_j) + \sum_{V_j E_i} \mathbf{F}(V_j, E_i), \tag{39}$$

and the torque $\boldsymbol{\tau}_{ij}$ of particle i is:

$$\boldsymbol{\tau}_{ij} = \sum_{V_i E_j} (\mathbf{p}(V_i, E_j) - \mathbf{c}_i) \times \mathbf{F}(V_i, E_j) + \sum_{V_j E_i} (\mathbf{p}(V_j, E_i) - \mathbf{c}_i) \times \mathbf{F}(V_j, E_i), \tag{40}$$

where $\mathbf{c}_i$ is the center of mass of particle i and $\mathbf{p}$ is the point of contact, which is defined as the middle point of the overlap area between a vertex and an edge:

$$\mathbf{p}(V, E) = \mathbf{X} + \left(a_i - \frac{1}{2} \delta(V, E) \right) \frac{\mathbf{X} - \mathbf{Y}}{\|\mathbf{Y} - \mathbf{X}\|}, \tag{41}$$

where $\mathbf{X}$ is the position of the vertex V, and $\mathbf{Y}$ is its closest point on the edge E. The movement of the center of mass r_i and the orientation φ_i of the particle are governed by the equations of motion:

$$m_i \ddot{\mathbf{c}} = \sum_j \mathbf{F}_{ij}, I_i \ddot{\boldsymbol{\varphi}} = \sum_j \boldsymbol{\tau}_{ij}, \tag{42}$$

where m_i and I_i are the mass and moment of inertia of the particle, respectively; the linear elastic model is used throughout this article. The force $\mathbf{F}$ can be written as:

$$\mathbf{F} = k_n \delta_n \mathbf{N} + k_t \delta_t \mathbf{T}, \tag{43}$$

where k_n and k_t are the normal and tangential stiffness, respectively; $\mathbf{N}$ and $\mathbf{T}$ are the normal and tangential unit vectors that are measured at the edge of the contact; δ_n denotes the length of the overlap; δ_t is the tangential relative displacement between two particles, which accounts for frictional forces. It is limited by the condition $k_t \delta_t \leq \mu k_n \delta_n$, where μ is the friction coefficient.

4 | COUPLING OF MPM AND SDEM

MPM and SDEM are fully coupled through the contact force information. The crucial part of the coupling is how to properly detect and calculate the contact force between the material points and SDEM particles. Liu et al[25] proposed a method that attaches material points to the DEM particles; the square particles are represented with nine materials at its corners, edges' middle point, and center of mass. Both the contact detection and contact forces are then calculated using a pure MPM contact algorithm developed by Bardenhangen and Brackbill.[14] This coupling method unifies the contact handling under a pure MPM scheme. The fundamental reason for these problems rises from the simplification of the contact and the dependency of the grid system. The contact force cannot be accurately calculated if only a small amount of material points is involved. However, the advantage of efficiency largely decreases if the material points are densely attached to the DEM particle.

4.1 | Contact handling between MPM and SDEM

In this article, we proposed a different approach for the computation of contact handling, which unifies the contact detect and force calculation under the scheme of SDEM. The basic idea of this algorithm can be summarized as follows. The Verlet distance, which is the cut-off distance for the potential contact between two discrete elements, is applied to examine the contact between material points and SDEM particles. If a material point is within the Verlet distance of a spheropolygon particle it is treated as a small SDEM disk particle with a certain radius for contact detection. If the material points and spheropolygon particles are in contact, the contact force between the material point and the spheropolygon is calculated based on DEM contact force models. The calculated force is applied to the material points in a form of extra boundary force term.

As indicated in Figure 4A, material points within the Verlet distance V_d are transformed into a circular discrete element with its position $\mathbf{x}_p$ as the center of mass. Here we name it *identified material points* (IMP). The interactions among the IMPs are still calculated under the MPM scheme despite the intersections of their radius that may happen after the transformation. Figure 5A shows that the magnitude of the contact force $\mathbf{f}^{\text{SDEM}}$ between an IMP and an SDEM particle can be then calculated based on the modification of Equation (39):

$$\xi(\mathbf{x}_p, E) = \langle a_i + r_p - d(\mathbf{x}_p, E) \rangle, \tag{44}$$

where r_p is the contact radius assigned to an IMP; a_i is the sphero-radius of the SDEM particle; d denotes the Euclidean distance between the points $\mathbf{x}_p$ and the edge E on the SDEM particle. The optimal value of r_p is still an open question. Here we provide an estimated interval for r_p:

$$l_p \sqrt{1/n} < r_p < l_p, \tag{45}$$

where l_p is the length of the background grid and n is the average number of the material point in each grid. The value of r_p must be smaller than the grid length to control the contact happens within or at the boundary of a cell. Meanwhile, it should be larger than the influential length that a material point representing in the computational domain.

If an IMP is in contact with multiple SDEM particles, as shown in Figure 5B, the particle-spheropolygon forces are summed together. The single contact of IMP is most likely to happen during the coupling since the radius assigned to the

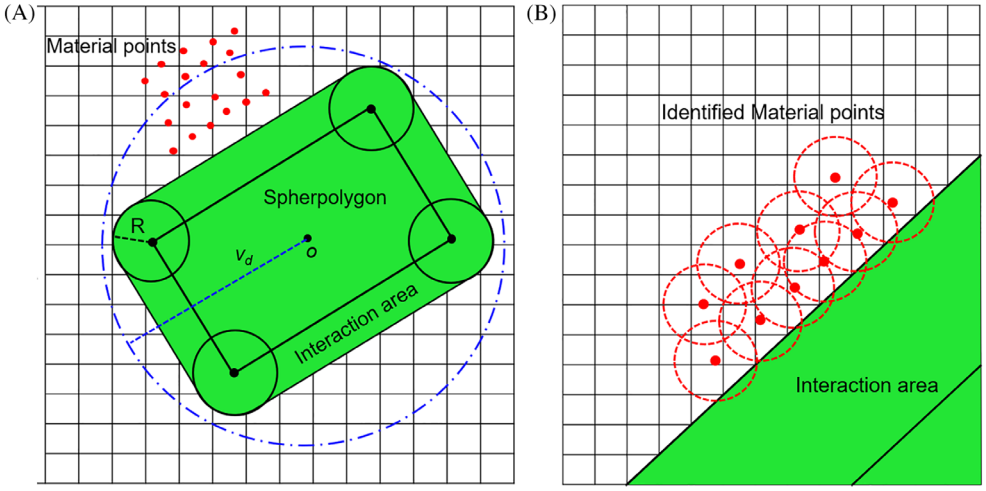

FIGURE 4 The contact handling between the spheropolygon and material points. A, Spheropolygon is represented by the green zone and material points by red points, V_d is the Verlet radius from the center of mass *o*. B, Material points in potential contact with the spheropolygon are assigned with a small radius (red dash circles) [Color figure can be viewed at wileyonlinelibrary.com]

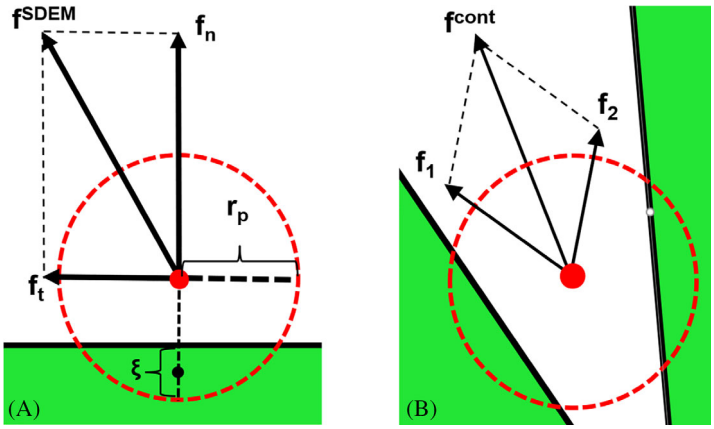

FIGURE 5 The intersection and contact force calculation between an identified material point (IMP) and spheropolygon discrete element method (SDEM). A, The calculation of the contact force between one IMP and SDEM particle. B, The total forces exert on an IMP [Color figure can be viewed at wileyonlinelibrary.com]

IMP is much smaller than the size of SDEM particles. But in extreme cases, such multiple contact relationship will not affect the stability or the efficiency of the coupling.

The contact forces are applied at the corresponding material point as an external boundary force:

$$\mathbf{f}_p^{\text{cont}} = \sum \mathbf{f}_k^{\text{SDEM}}, \tag{46}$$

$$\mathbf{f}_I^{\text{cont}} = \sum_p \mathbf{f}_p^{\text{cont}} S_{Ip}(\mathbf{x}_p), \tag{47}$$

where the $\mathbf{f}^{\text{SDEM}}$ is the coupling contact force; $\mathbf{f}_p^{\text{cont}}$ and $\mathbf{f}_I^{\text{cont}}$ are the external force on the IMPs and corresponding nodes, respectively. Therefore, the nodal equation of motion (Equation 18) is further modified as:

$$\dot{\mathbf{p}}_I = \mathbf{f}_I^{\text{int}} + \mathbf{f}_I^{\text{ext}} + \mathbf{f}_I^{\text{cont}}. \tag{48}$$

In this way, the influence of the contact force is taken into the calculation of MPM at step (c). And through this equation, it could further its influence on the movement of material points in the whole computational area. For the SDEM particle, the contact forces are applied at its center of mass. The total force and torque exerted on the particle in Equations (39) and (40) are now modified as:

$$\mathbf{F}_{ij} = \sum_{V_iE_j} \mathbf{F}(V_i, E_j) + \sum_{V_jE_i} \mathbf{F}(V_j, E_i) + \sum_p \mathbf{f}^{\text{SDEM}}(V_i, \mathbf{x}_p) + \sum_p \mathbf{f}^{\text{SDEM}}(\mathbf{x}_p, E_i), \tag{49}$$

$$\boldsymbol{\tau}_{ij} = \sum_{V_i E_j} (\mathbf{p}(V_i, E_j) - \mathbf{c}_i) \times \mathbf{F}(V_i, E_j) + \sum_{V_j E_i} (\mathbf{p}(V_j, E_i) - \mathbf{c}_i) \times \mathbf{F}(V_j, E_i) + \sum_p (\mathbf{p}(V_i, \mathbf{x}_p) - \mathbf{c}_i) \times \mathbf{f}^{\text{SDEM}}(V_i, \mathbf{x}_p) + \sum_p (\mathbf{p}(\mathbf{x}_p, E_i) - \mathbf{c}_i) \times \mathbf{f}^{\text{SDEM}}(\mathbf{x}_p, E_i). \tag{50}$$

These equations are equal to adding extra contact forces that are produced by small circular particles to the large SDEM particle, so that the movement and rotation of the SDEM particles are also affected by the IMP that is in contact with it.

Since the algorithm is using an explicit form, the critical time step $\Delta t_{\min}$ needs to be determined for the stability of the coupling. This criterion[42] can be written as:

$$\Delta t_{\min} = \min \begin{cases} \kappa_1 \frac{l_{\min}}{c_{\max}} \\ 2\pi\kappa_2 \sqrt{\frac{m_{\min}}{k_n}} \end{cases}, \tag{51}$$

where the $l_{\min}$ is the minimum length of the background grid and $c_{\max}$ is the maximum acoustic velocity of the material in MPM; $m_{\min}$ is the minimum mass of the SDEM particle. The coefficient κ_1 and κ_2 are used to further guarantee the stability since the equation for critical time step is obtained based on the linear elasticity, which $\kappa_1 = 0.8$ and $\kappa_2 = 0.1$ are commonly used.

The contact between material points and the SDEM particle can be fully coupled together through the contact force. There are several advantages to using this scheme. Contact relations are detected with the Euclidian distance between the center of mass of SDEM particle and the position of a material point. The contact list can be saved as a data structure and reused for the next time step if the displacement of the particles and material points is small. It is more efficient than the condition of a mutual grid node where the velocity field on each object is constantly recalculated. Contact forces can be directly calculated with DEM contact models instead of using the grid momentum as an indirect approach. Positions for applying contact forces are not restricted by the grid node or the geometrical nodes of the rigid particles. Irregular shapes are considered, and the angular momentum of the rigid body is better preserved.

4.2 | Coupling method procedures

The coupling algorithm in a time step Δt can be summarized as follows:

1. *SDEM*: contact detection and force calculation

   Update the contact list of SDEM particles based on the Verlet distance.
   Update the contact list of SDEM particles and IMPs.
   Update Vertices $\{V\}$ for each particle.
   Update the vertex-edge contact relations between particles within the contact list.
   Calculate the contact force of SDEM particles and apply the gravity.
   Calculate the $\mathbf{f}^{\text{SDEM}}$ between SDEM particles and IMPs.

2. *MPM*: variables transfer between nodes and points

   Calculate the nodal mass m_I, momentum $\mathbf{p}_I$ and $\mathbf{v}_I$.
   Calculate the strain and spin rate $\dot{\boldsymbol{\varepsilon}}_p$, $\dot{\boldsymbol{\Omega}}_p$ of material points.
   Calculate the stress $\boldsymbol{\sigma}_p$ of material points.

3. *Coupling*: Update of material points

   Calculate the nodal force $\mathbf{f}_I^{\text{ext}}$, $\mathbf{f}_I^{\text{int}}$, and coupling force $\mathbf{f}_I^{\text{cont.}}$.
   Update the nodal momentum $\mathbf{p}_I$.
   Update the position $\mathbf{x}_p$ and velocity $\mathbf{v}_p$ of material points.

TABLE 1 Parameters and material properties for the simulation of conservation of energy

SDEM parameters				MPM (GIMP) parameters			
k_n	Normal stiffness	6.0×10^6	N/cm	d_g	Grid interval	0.3	cm
k_t	Tangential stiffness	3.0×10^5	N/cm	r_p	Coupling radius	0.1	cm
μ	Frictional coefficient	0.1		n	Number of points	5000	
Δt	Time interval	1.0^{-4}	s	MPM material properties			
V_d	Verlet distance	0.2	cm	ν	Poisson's ratio	0.278	
a_i	Sphero radius	2.0	cm	K	Bulk modulus	5.0×10^2 / $\times 10^3$	KPa
SDEM material properties				G	Shear modulus	3.7×10^2 / $\times 10^3$	KPa
ρ_d	Density	2.0	g/cm^2	ρ_p	Density	2.0	g/cm^2

Abbreviations: GIMP, generalized interpolation material point; MPM, material point method; SDEM, spheropolygon discrete element method.

4. *Coupling*: Update of the SDEM particles

   Apply the $\mathbf{f}^{\text{SDEM}}$ to the SDEM particles.
   Update the velocity, angular momentum.
   Update the position of center of mass for each SDEM particles.

5 | VERIFICATION

A series of tests is conducted in this section for the validation of MPM-SDEM method. They include three essential parts of the interaction between MPM and SDEM bodies: the conservation of energy, the contact force, and the granular-solid interaction. The first two tests are simulated using linear elasticity as the material property of the MPM; the last test is conducted with Drack-Prager model for the plastic deformation of granular material. The conservation of energy is crucial for the stability of the coupling. Contact forces between the MPM and SDEM bodies need to be correct since the contact handling method is unified under the DEM contact. It is also necessary to examine the plastic behavior between the MPM and SDEM where the variation of contact relationships is far stronger than that of solid cases. Results are rigorously compared and analyzed with analytical solutions. It helps to better understand the advantages and limitations of this method as a general scheme for the coupling between SDEM and MPM.

5.1 | Conservation of energy

Two tests are designed to investigate the exchange of momentum and the transferring between the kinetic and gravitational potential energy. The main purpose is to examine whether the energy of the system is conserved by the collision between MPM and SDEM. The stability of the simulation can only be preserved if no extra energy is introduced into the system by the coupling algorithm. The other important purpose is to investigate whether the coupling could well preserve the conservation of energy and how strong will the coupling affects the system energy. The system still has the numerical dissipation caused by pure DEM and MPM.

5.1.1 | Exchange of momentum

The exchange of momentum is conducted by the 2D-elastic collision between MPM and SDEM disks. As illustrated in Figure 6, the MPM disk moving with a constant velocity of 2 m/s toward the SDEM body, which is in a static state. The disks have the exact same shape, density, and size. The effect of gravity is eliminated from this test. Material properties and simulation parameters are listed in Table 1.

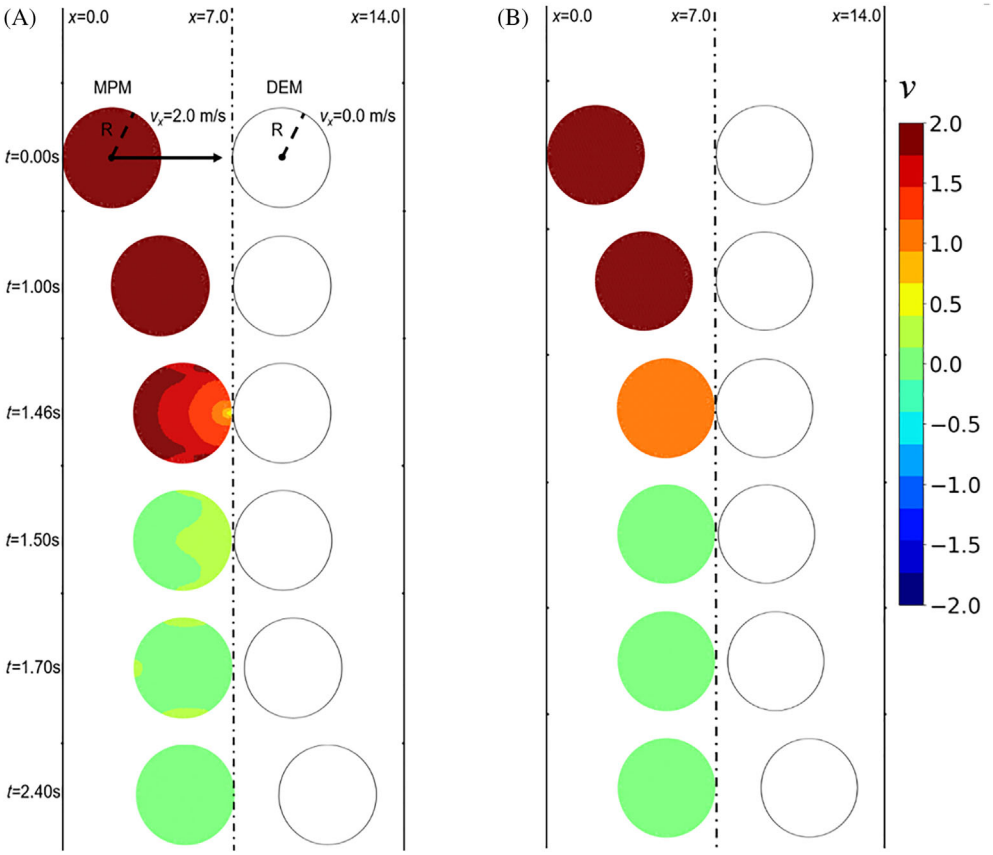

FIGURE 6 The collision between the material point method (MPM) and discrete element method (DEM) disk at each time slice (unit: cm/s). A, The soft material case. B, The hard material case (color encodes velocity) [Color figure can be viewed at wileyonlinelibrary.com]

The MPM and SDEM share the same time interval and sequence; the coupling parameters for the collision handling are calculated with the same parameter of normal and tangential stiffness of SDEM. Two groups of material modulus, which are marked bold in Table 1, are used for the MPM disc. The bulk and shear modulus of the hard group is 10 times larger than that of the soft case. This comparison is proposed to investigate the influence of the material properties on the conservation of energy. It could further demonstrate the ability of MPM-SDEM to simulate the soft-rigid multibody system.

It can be observed from Figure 6A that the contact between two bodies is captured by the coupling algorithm and the collision is calculated with the contact force. The velocity of the MPM disk drops rapidly during the collision and transfers its kinetic energy to the DEM disk at $t = 1.46$ seconds and 1.50 seconds. Part of the energy is stored in the MPM body in a form of strain energy because some of the material points at $t = 1.70$ seconds still have a small velocity. This part of the energy is dissipated in the MPM disk since the collision is completed. It dissipated due to the *P-G* transferring scheme and eventually disappear (eg, $t = 2.4$ seconds). This phenomenon is consistent with the variation of square of v in Figure 7, where kinetic energy is largely transferred into the DEM disc, which obtained a $v_x = 1.92$ m/s. It still shows a 7.84% loss of kinetic energy as these parts are not transferred to DEM after the collision.

For the hard material case in Figure 7, the conservation of energy is much better than that of the soft case. The collision happened in a short time of duration as it is shown in Figure 6B after $t = 1.46$ seconds. The velocity of the material points disk becomes zero after the collision. The SDEM disk obtained a $v = 1.992$ m/s. The kinetic energy reaches a level of 99.202% of the perfect elastic collision.

5.1.2 | Transferring between the gravitational potential and kinetic energy

The test for the potential-kinetic energy transferring is conducted by dropping an MPM elastic disk at the spheropolygon boundary. The spheropolygon element is set as an unmoveable elastic boundary. It can be seen in Figure 8 that the MPM disk hits the boundary and bounces back at the spheropolygon boundary. The contact is detected by the algorithm and

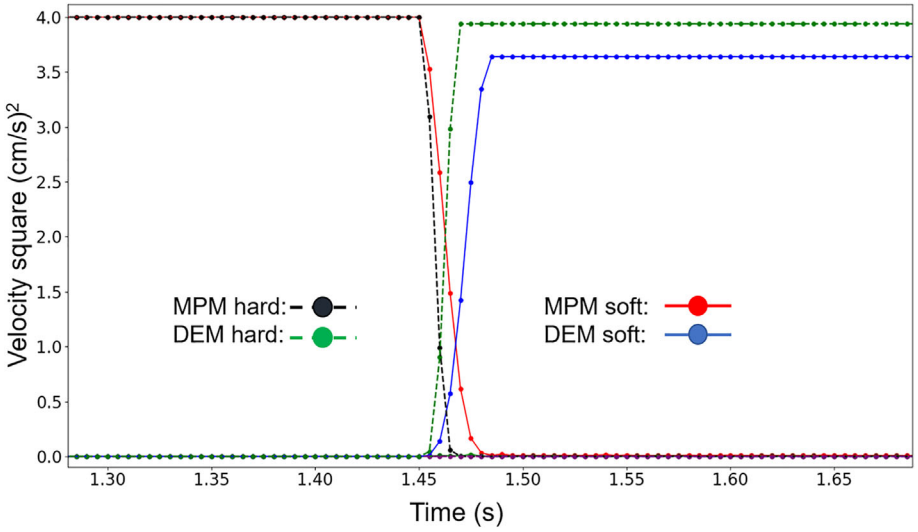

FIGURE 7 The variation of velocity square of discrete element method (DEM) and material point method (MPM) disk with different material properties [Color figure can be viewed at wileyonlinelibrary.com]

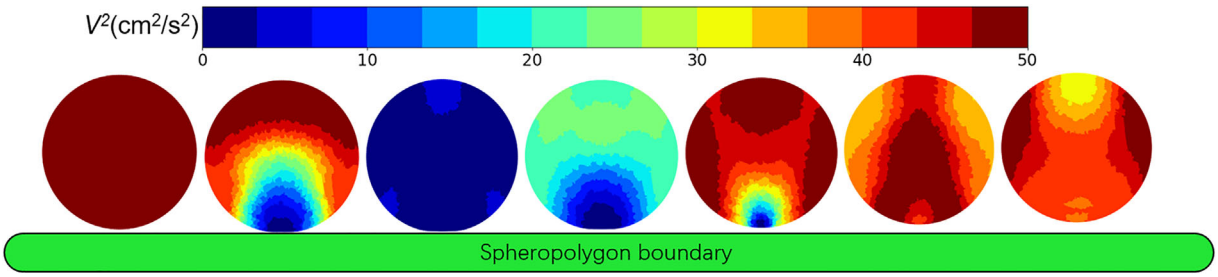

FIGURE 8 The soft elastic disk dropping at and bouncing back by the spheropolygon boundary [Color figure can be viewed at wileyonlinelibrary.com]

the collision is properly calculated. The simulation parameters and material properties are the same as in Table 1; the gravitational acceleration is -10.0 cm/s.^{2}

The variations of the vertical velocity square are presented in Figure 9. The hard disk is shifted with +0.5 second on the time axis for the comparison. Figure 9 indicates that the soft discs still have a 6.947% loss of energy after the collision. Similarly, the hard disk has a better performance for the conservation of energy; less energy is dissipated during the collision, and the maximal kinetic energy reaches 98.95% the initial potential energy. It can also be observed from Figure 10 that soft disk experienced a longer time to complete the transferring between kinetic and potential energy. For both soft and hard disc, no extra energy is generated by the collision since the squared velocity after the collision is lower than the analytical limit. It indicates the coupling algorithm can maintain its stability. These results further support the fact that the material modulus has a certain influence on the conservation of energy. The low value of elastic modulus could generate a strong loss of energy after the coupled collision. It may cause a problem for the simulation that requires a high velocity (eg, impact engineering) but could still be well-applied for the simulation of quasi-static or low-velocity issues.

5.2 | Coupling force

The coupling of the MPM and SDEM is conducted through the contact force that calculated based on the contact model of DEM. It distinguishes the coupling method developed in this paper from the existing method, which can be used for the quasi-static and dynamic cases. The value of normal and frictional coupling force between the MPM and SDEM are examined in this section. Especially the contact force's dependence on the grid size is investigated here with four different values of grid interval. Simulation parameters and material properties are given in Table 2; integer i denotes the variation of the grid size, which ranges from 0 to 3 and marked in bold.

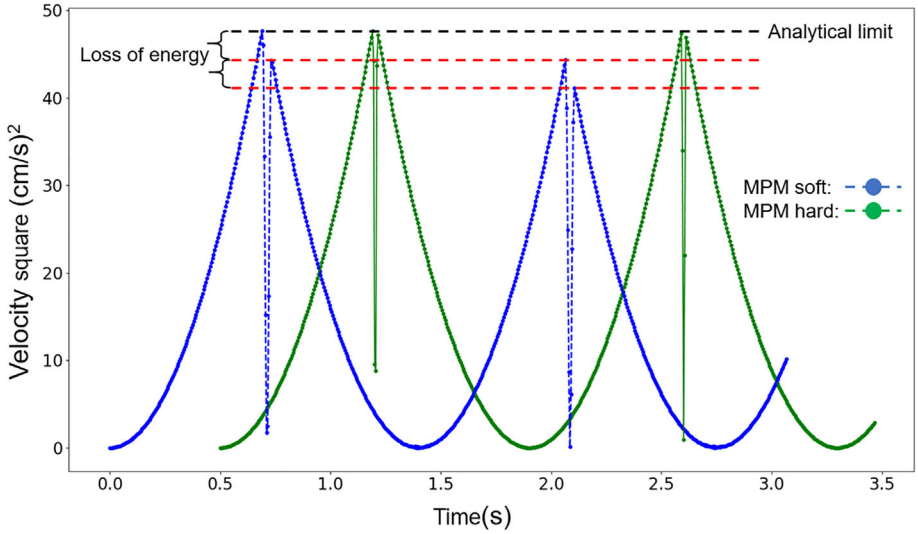

FIGURE 9 The change of velocity squared of the material point method (MPM) disc; the hard disk is shifted with a 0.5 second on the time axis for the comparison [Color figure can be viewed at wileyonlinelibrary.com]

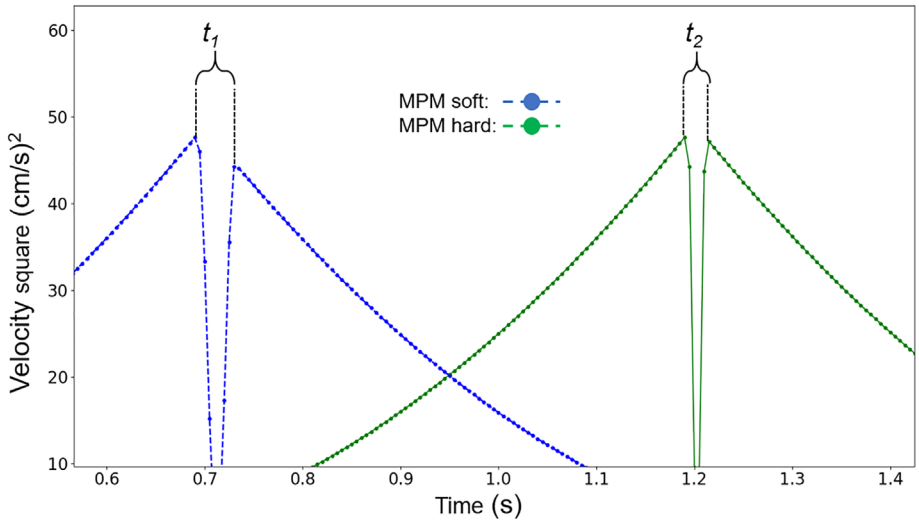

FIGURE 10 The time gap t_1 and t_2 of collision obtained with soft and hard material point method (MPM) disk cases [Color figure can be viewed at wileyonlinelibrary.com]

5.2.1 | Normal force

The normal contact force is examined by placing an MPM elastic square on the spheropolygon boundary. Reaction forces are generated due to the gravitational force and, based on the coupling algorithm, applied on each material point at the bottom of the square. Figure 11 indicates that the contact relations between material points and the boundary are properly captured; the contact force is equally applied at the points that are in contact with the spheropolygon boundary. There are in total 51 material points near the boundary and each one has a normal force of 0.4902 N normal force as the reaction force for the gravity.

The total reaction force for different grid sizes is shown in Figure 12. It indicates that the simulated value of normal force has a strong vibration at the beginning of the simulation. Such vibration is caused by the initial zero-overlapping configuration between the boundary and the elastic block. The normal force gradually converges to the analytical solution. The progress indicates that the static equilibrium is searched by the contact algorithm and eventually reached. The kinetic energy is dissipated due to the viscoelastic contact model of DEM and the numerical damping within the point-grid transferring scheme of MPM. The energy dissipation here is a positive factor, which helps the system to reach a static state and provides the correct force information. This tendency can be observed for all four cases with different grid sizes. The larger size of the grid only improves the intensity of the energy dissipation but does not change the convergence of the contact force; the correctness of the contact force is independent of the size of the background grid. The MPM and SDEM can be properly coupled through the DEM contact scheme.

TABLE 2 Parameters and material properties for the simulation of MPM-SDEM contact force

SDEM Parameters				MPM (GIMP-PIC) Parameters			
k_n	Normal stiffness	6.0×10^6	N/cm	d_g	Grid interval	$0.35 + 0.05 \times i$	cm
k_t	Tangential stiffness	3.0×10^5	N/cm	r_p	Coupling radius	0.1	cm
μ	Frictional coefficient	0.1		n	Number of points	2601	
Δt	Time interval	2.0^{-4}	s	MPM material properties			
V_d	Verlet distance	0.2	cm	ν	Poisson's ratio	0.2558	
a_i	Sphero radius	0.5	cm	K	Bulk modulus	6.0×10^3	KPa
General Parameter				G	Shear modulus	3.5×10^3	KPa
g	Gravitational acceleration	100.0	cm/s^2	ρ_p	Density	2.5	g/cm^2

Notes: Integer i, which denoted in bold, ranges from 0 to 3 to consider four different grid sizes.
Abbreviations: GIMP, generalized interpolation material point; MPM, material point method; PIC, particle-in-cell; SDEM, spheropolygon discrete element method.

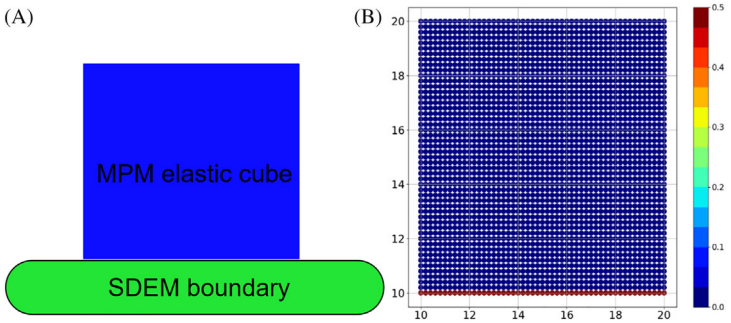

FIGURE 11 Normal forces generated between the elastic material point method (MPM) block and spheropolygon boundary (unit: N); $d_g = 0.35$ and $t = 3.5$ seconds. A, The normal force contact test of MPM cube and spheropolygon discrete element method (SDEM) boundary. B, The normal forces are generated at the bottom of the MPM elastic square where the material points are in contact with the spheropolygon boundary and the magnitude of the force generated each point is all equal to 0.4902 N (red value in color bar); the other material points have zero force value (blue value in color bar) since they are not in contact with the boundary [Color figure can be viewed at wileyonlinelibrary.com]

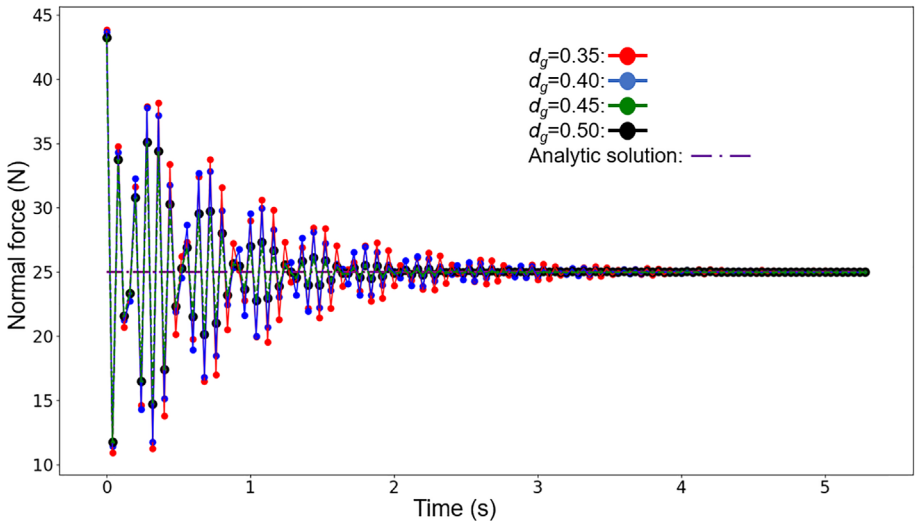

FIGURE 12 The total normal force vs time for different background grid size d_g [Color figure can be viewed at wileyonlinelibrary.com]

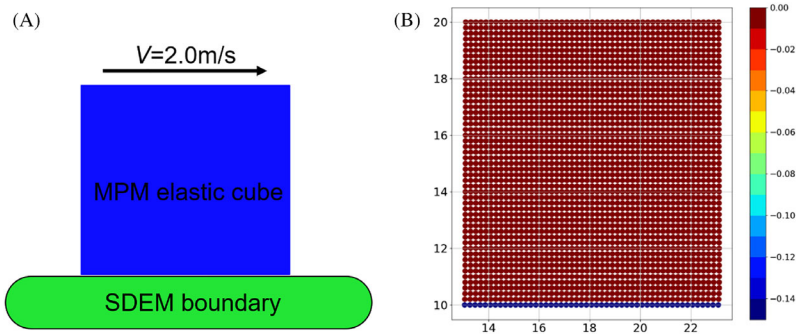

FIGURE 13 Frictional forces generated between the elastic material point method (MPM) block and spheropolygon boundary (unit: N); $d_g = 0.35$ and $t = 3.5$ seconds. A, The normal force contact test of MPM cube and spheropolygon discrete element method (SDEM) boundary. B, The frictional forces are generated at the bottom of the MPM elastic square where the material points are in contact with the spheropolygon boundary while sliding; the magnitude of the frictional force on each point are all equal (blue value in color bar) since their relative position to the boundary is the same; the other material points have zero frictional force (red value in color bar) since they are not in contact with the boundary [Color figure can be viewed at wileyonlinelibrary.com]

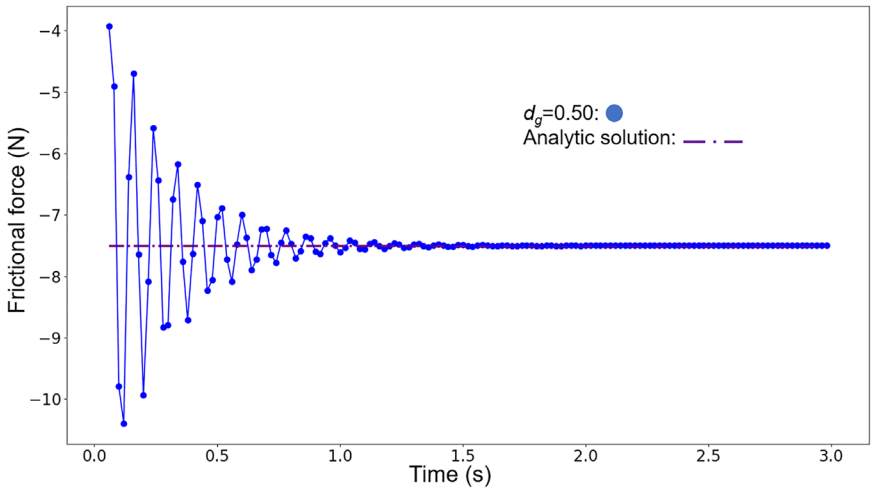

FIGURE 14 The total frictional force vs time for grid size $d_g = 0.5$ [Color figure can be viewed at wileyonlinelibrary.com]

5.2.2 | Frictional force

The same model is used for simulating the frictional force. A constant velocity of $V_x = 2.0$ m/s is applied to the same MPM square. It is sliding toward the positive direction of the x-axis and generates a friction force. Its friction coefficient between the MPM and DEM boundary are set as $\mu = 0.3$. It can be observed from Figure 13 that the friction force applies to the material points located at the bottom of the elastic MPM square. The magnitude of the friction force is $\mu F_n = -7.5$ N, which equals -0.14706 N for each material point that in contact with the boundary. This result is consistent with the result of the normal-force test.

The variation of total frictional force is shown in Figure 14. The test for the effect of grid size has been clarified in the normal force test and therefore not repeated here. The grid size $d_g = 0.50$ is used to quickly reduce the vibrations generated by the initial configuration. Similarly, the friction force also converges to the analytical value with the progress of the simulation. The vibration energy is dissipated and the MPM square reaches a quasi-static state; both normal and friction force are correctly calculated.

5.3 | Granular flow

The coupling performance between the SDEM and the MPM granular material is tested with the silo flow model. The Drucker-Prager model is used to simulate the plastic behavior of the noncohesive dry sand, which is represented

TABLE 3 Parameters and material properties for the simulation of MPM-SDEM granular flow

SDEM parameters				MPM (APIC) parameters			
k_n	Normal stiffness	6.0×10^6	N/cm	d_g	Grid interval	0.35	cm
k_t	Tangential stiffness	3.0×10^5	N/cm	r_p	Coupling radius	0.1	cm
μ	Frictional coefficient	0.2		n	Number of points	$8/9/10 \times 10^3$	
Δt	Time interval	2.0^{-4}	s	MPM material properties			
V_d	Verlet distance	0.2	cm	ν	Poisson's ratio	0.2358	
r_d	Sphero radius	0.5	cm	K	Bulk modulus	5.0×10^2	KPa
General Parameter				G	Shear modulus	3.2×10^2	KPa
g	Gravitational acceleration	10.0	cm/s^2	ρ_m	Density	1.5	g/cm^2
Drucker-Prager model							
σ_t	Tensile strength	0.0	MPa	Φ	Friction angle	35.0	degree
ψ	Dilation angle	25.0	degree				

Abbreviations: APIC, affine-particle-in-cell; GIMP, generalized interpolation material point; MPM, material point method; SDEM, spheropolygon discrete element method.

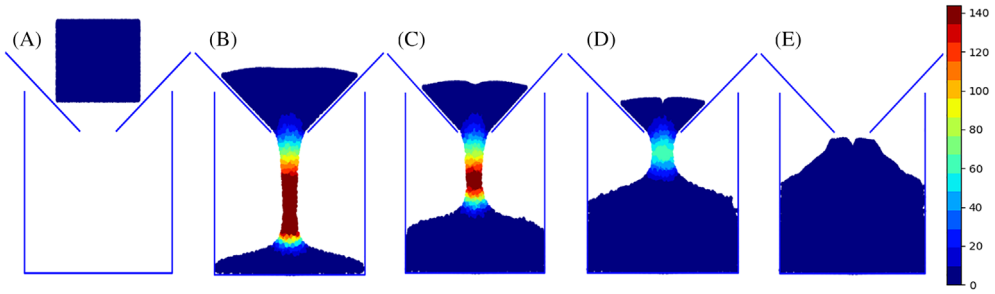

FIGURE 15 Four different stages of silo flow. Material point method (MPM) is used to represent the granular material. The silo and container are spheropolygon discrete element method (SDEM) particles. The color bar encodes the square velocity of the granular materials (unit: cm^2/s^2) The diameter of the neck is $D_0 = 0.04$ m. Snapshots are taken at, A, $t = 0.0$ second, B, $t = 3.0$ seconds, C, $t = 5.0$ seconds, and D, $t = 10.0$ seconds [Color figure can be viewed at wileyonlinelibrary.com]

with MPM. The SDEM is used as the silo and container of the granular flow. Five different diameters of the silo neck are used to compare the results with the 2D Beverloo law.[43] The main reason for conducting these tests is because the contact relationship for the plastic MPM-SDEM case is far more changeable than that of elastic MPM-SDEM cases. Contacts are constantly generated and deleted in the granular flow. Therefore, it is necessary to test whether the coupling simulation is reliable. Material points, although representing a continuous area, are used to approximate the assemble of discrete bodies (ie, sand or rock pile). Three different numbers of material points are used to investigate its influence on mass transportation. The simulation parameters and material properties are given in Table 3.

As illustrated in Figure 15, the MPM dry sand flows through the bottleneck of the silo and reaches a steady flowing state; the sand drops at the bottom and held by the SDEM container. It indicates that the coupling algorithm remains stable for the granular material. The contact can be effectively detected and properly handled.

The mass transfer rates for different sizes of the silo neck are shown in Figure 16. Simulations with different numbers of material points are performed for each diameter. Results indicate that the simulated mass transfer rates agree well with the analytical solution of the 2D Beverloo law.[44] The rate increases with the increase in the diameter in a 3/2 power law relation. The number of material points does not have a strong influence on the results since MPM is a continuous numerical method. Although there is still a deficiency for using the Drucker-Prager model as indicated earlier, the coupling method is reliable for simulating granular-solid interaction.

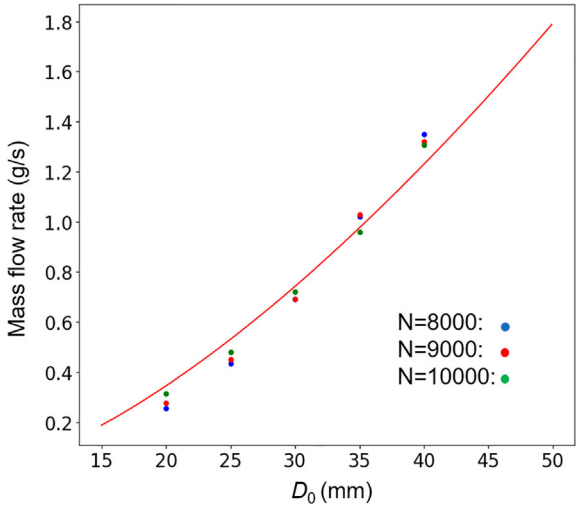

FIGURE 16 The mass flow rate $M = C\rho g^{0.5}(D_0 - k_c r_p)^{1.5}$ for different silo neck diameter and number of material points; $C = 0.58$ and $k_c = 2.2$ are the empirical coefficient; D_0 is the diameter of the silo neck [Color figure can be viewed at wileyonlinelibrary.com]

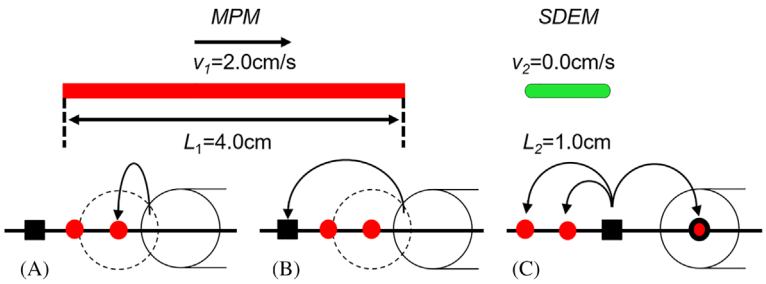

FIGURE 17 The one-dimensional rod collision test and the contact force scheme. The material point is denoted with the red dot and the grid node represented with the black square. The red rod is represented with 400 material points and assigned with an initial velocity $v_1 = 2.0$ cm/s; the lime rod is the rigid spheropolygon discrete element method (SDEM) particle. A, MPM-SDEM scheme, the coupling force is applied at the material point. B, MPM-GRID scheme, the coupling force is applied at the corresponding node in the vicinity of the contact position. C, The MPM-DEM method, the rigid body is represented with material points (black ring circle is the left tip of the rigid body), the coupling is calculated at the node and applied to the material points [Color figure can be viewed at wileyonlinelibrary.com]

5.4 | Comparison of the contact schemes

A series of numerical tests based on the one-dimensional elastic rod collision is conducted to compare the grid dependency of different contact schemes, and further, illustrates the advantages of MPM-SDEM. The parameters in Table 1 is adopted with 400 material points and the equal mass of two rods. The basic model and three contact handling schemes are shown in Figure 17. The left scheme is the MPM-SDEM where the coupling force is calculated through the DEM contact model and applied at the corresponding material point (Equations (46) and (47)); The MPM-GRID scheme in the middle has the same way of calculating the coupling force but applies the force directly at the corresponding node. The last coupling scheme (MPM-DEM) is proposed by Liu et al where the rigid body part is represented with three material points at the tips and the middle point (red circle with the black ring), the coupling force is calculated through the MPM contact model[17] at the mutual node.

The grid size ranges from 0.1 to 1.0 cm with a variation of 0.1 cm for each test. The accuracy is measured with the velocity squared v^2 of the system before and after the collision. The results for each scheme are shown in Figure 18. It can be observed that all three schemes have a general grid dependency; a smaller grid size provides better conservation of kinetic energy of the system, which indicates a more accurate description of coupling between the MPM and rigid body. MPM-SDEM shows the best performance. The accuracy increases linearly with the decrease in grid size at the logarithmic scale. A proper accuracy is provided even at the extreme case where the grid size equals the size of the rigid rod ($L_2/d_g = 1.0$). The MPM-GRID and the MPM-DEM scheme has distinctively higher errors at the large grid size ($L/d_g = 1.0$-0.5). Both schemes show a similar pattern of grid-dependency and rapidly merging to the accuracy of

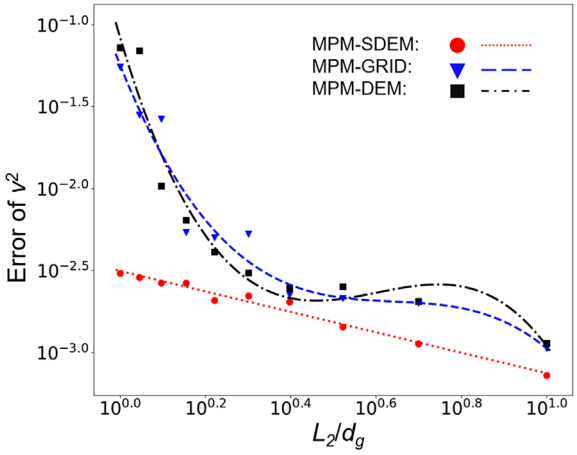

FIGURE 18 The grid-dependency of error v^2 for each coupling scheme. The fitting lines are generated with the standard polynomial regression; linear regression for material point method-spheropolygon discrete element method (MPM-SDEM) and cubic regression for the other two schemes [Color figure can be viewed at wileyonlinelibrary.com]

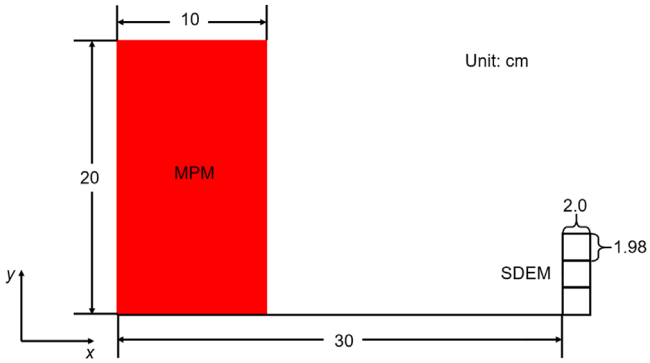

FIGURE 19 The initial configuration of the granular flow and spheropolygon discrete element method (SDEM) blocks [Color figure can be viewed at wileyonlinelibrary.com]

MPM-SDEM. The difference between the three cases becomes minimal at $d_g = 0.1$ cm, which is also the limitation of optimal r_p of IMP in Equation 45.

6 | VALIDATION

The motion of wooden blocks under the impact of the granular flow is simulated in two dimensions. This test was originally conducted by Liu et al[25] for the validation of a coupled MPM-DEM method. In their method, each DEM block is represented by nine visual material points to couple its interaction with MPM granular flow based on the exchange of momentum. The configurations of the test are given in Figure 19. The granular flow will be released and impact three piled-up wooden blocks. For the granular material, the gravitational potential is transferred to the kinetic energy and eventually exerts on the blocks through the point-grid projection on the mutual background grids. Two upper blocks will be pushed to the right side and obtain angular momentum; Block.3 is glued to the ground and thus unmovable. The variation of the rotational angle of block No.2 is recorded and compared with experimental data.

In this section, this test is reconducted using our MPM-SDEM coupling scheme. The results are compared and rigorously analyzed with both numerical and experimental data from the existing literature. It further illustrates the advantages of using the contact force as the connection of the coupling between MPM and DEM. The material properties and simulation parameters are given in Table 3 with a few modifications for the simulation: $g = 10$ m/s, $\psi = 0°$, $n = 8000$, and ϕ=22.0° to be consistent with Liu et al's test.

The movements of granular flow and blocks in the simulation are shown in Figure 20. Each screenshot is taken at the exact same time as Liu et al's study to provide a clear visual comparison. The results indicate that both the collapse of the granular pile and the motion of the blocks agree well with the existing numerical and the experimental data at each compared time step. The sand flow reaches the pile of blocks at $t = 2.5$ seconds; the blocks start to move and rotate due to the impact. The block No.2 touches the ground after $t = 4.0$ seconds and block No.1 touches the ground after $t = 4.5$ seconds.

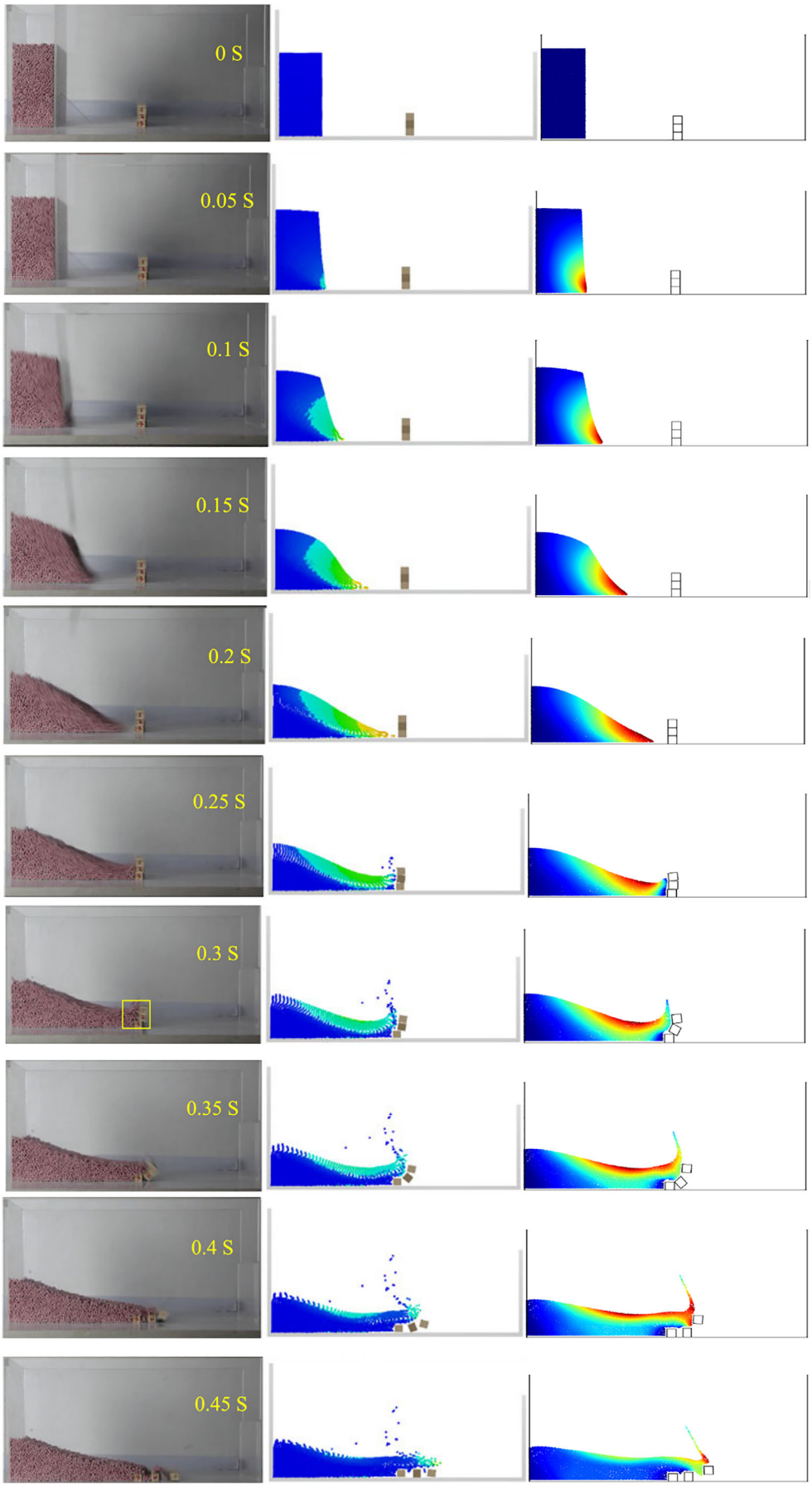

FIGURE 20 Comparison among Liu et al's experiment (left) and numerical results (middle), and material point method-spheropolygon discrete element method (MPM-SDEM) (right) simulation of granular flow impacting blocks at different time steps [Color figure can be viewed at wileyonlinelibrary.com]

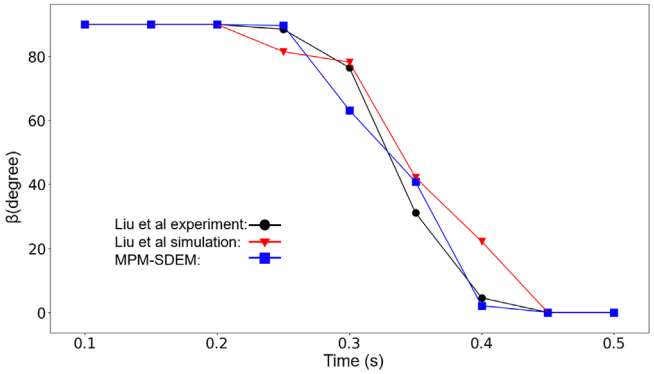

FIGURE 21 The temporal variation of block No.2's rotational angle β [Color figure can be viewed at wileyonlinelibrary.com]

The rotation of block No.2 is recorded and compared with the numerical and experimental data in Figure 21. It can be observed from the results that compared with the existing method, the rotational angle of MPM-SDEM is generally closer to the experimental results at each measured time step. Such better performance is particularly obvious at $t = 0.25$ and $t = 0.40$ second. The differences between MPM-SDEM and experimental data are smaller than 4.0°, where this difference reaches almost 20.0° for the existing method. Furthermore, the variational of the rotational angle experiment is smoother than that of Liu et al's method. It indicates that the change of the angular momentum and rotational angle of block No.2 is continuous in the experiment. But the result of the existing coupling method exhibits clear jumps of these variables. According to the snapshots, this kind of discontinuity is particularly strong between $t = 0.2$ second to 0.25 second.

Such a problem in Liu et al's method is caused by two reasons: first, the DEM blocks are insufficiently represented with only nine material points. There is a strong loss of accuracy when calculating the momentum transfer between the granular flow and the highly simplified DEM blocks. Second, this coupling scheme has a strong dependency on the background grid. The angular momentum will be highly compromised if the gird size is too large. However, if the grid size is too small the material point at the center of mass will be ignored and receive zero momentum from the granular flow. The grid size has a strong influence on the simulation, yet the optimal value is highly difficult to be determined; neither increase nor decrease in the grid size can guarantee an improved accuracy. Improvements can be made by increasing the number of material points to represent the DEM block. But it makes a large compromise of computational efficiency; the contact detection and farce calculation become far more expensive. Therefore, this method is only reliable for certain cases.

In contrast to the existing method, the displacement pattern provided by MPM-SDEM shows a more continuous trend that similar to the experimental data. No sudden jump of angular velocity for the SDEM blocks is observed. This is because the coupling is conducted through the contact force. Neither contact detection nor force calculation has a strong dependency on the grid. The angular momentum is better preserved during the impact process since the transferring of the momentum is not limited by the grid system. Contact detection and force calculation can be obtained using solely the Euclidian distance. Material points of the granular flow can transfer its kinetic energy to the edges of the blocks at any position if their Euclidian distance is recognized as in contact. The MPM-SDEM shows a better performance comparing to the existing method and should be reliable for a variety of applications due to its unique advantages.

7 | SIMULATION OF THE GRANULAR MATRIX

An important application of the MPM-SDEM coupling method is to simulate the granular matrix. It consists of particles in very different sizes and thus exhibits complicated physical properties different from a homogeneous state of its constituents. The size ratio between large particles and fines could reach a scale of $10^{5\text{-}6}$. The simulation of such a system is highly computational expensive using a pure DEM method. Numerical methods based on the continuum mechanics also have difficulties to simulate both of the large deformations of fines and the interaction among particles. Studies have been conducted using DEM and certain progress for understanding the granular matrix has been made.[1,45] However, particles and the fines are represented with a fairly limited amount; the mechanical properties of fines are not rigorously simulated. These problems deeply undermine the validity of conclusions.

The MPM-SDEM method provides a better way to simulate the micro-mechanism of the granular matrix since it is a scale-crossing method that could tolerant the objects in an extreme size ratio. A basic model is presented here for

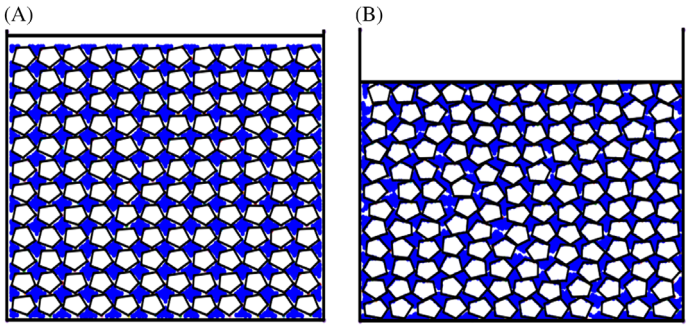

FIGURE 22 The uniaxial compression of the granular matrix consist of fines and particles. The container size of 61×61 cm; the compression bar is moving with a constant velocity of $v_y = -0.5$ cm/s. A, The initial configuration of the granular matrix. B, Granular matrix at $t = 22.0$ seconds [Color figure can be viewed at wileyonlinelibrary.com]

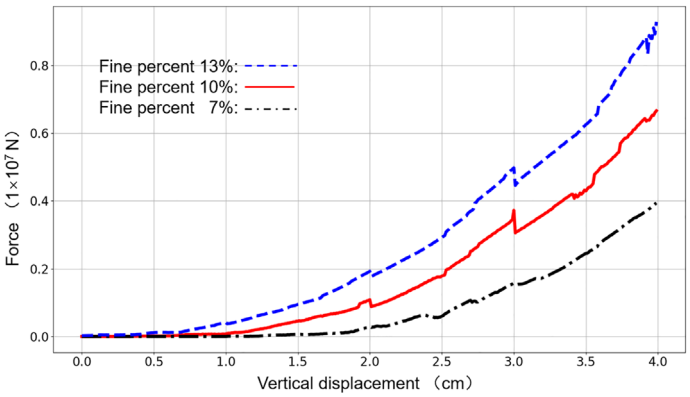

FIGURE 23 The force-settlement curve for different percentages of fine content [Color figure can be viewed at wileyonlinelibrary.com]

simulating the structure of granular matrix. Large particles are represented by the SDEM with randomly generated pentagons. Fines, which fills the voids between the particles, are simulated with the MPM. The mechanical properties of fines are governed by the *D-P* model. In this way, the influence of fines is rigorously simulated with a well-established constitutive model, while the discrete behavior of large particles can still be preserved. The uniaxial compression test is conducted to investigate the effect of the fine percentage in the granular matrix. The parameters are the same as Table 3 except the density of SDEM particles is changed to 2.2 g/cm^2.

The basic structure of the granular matrix sample is shown in Figure 22. The SDEM particles are the skeleton while MPM fines exist in the voids among them. Both of the components bear the compressive load from the top. At the early stage of loading, the compression mainly exerts on the SDEM particles since the void space is not fully saturated. SDEM particles will start to slowly move and rotate. This process can be regarded as a rearrangement process for the skeleton part of the granular matrix. The void space is shrinking due to this rearrangement. MPM fines start to carry the compressive load by interacting with SDEM particles if the void space is small enough. This phenomenon is one of the reasons that the granular matrix exhibits a relatively complex mechanical behavior.

The compression force-settlement curves are shown in Figure 23. The basic skeleton structure of the SDEM is preserved in each case. Because the void space is not saturated by fines and the skeleton structure thus will not be affected by a small change of fine content. It can be observed from the results that the fine percentage has a major impact on the compressibility of the granular matrix, which would further affect the result for measuring Young's modulus. Even though the variation is small, a higher fine percentage largely reduces the compressibility of the granular matrix and, therefore, exhibits a higher Young's modulus at the macroscale. This test provided a good demonstration of the potential application of MPM-SDEM method.

8 | CONCLUSIONS

A hybrid MPM-SDEM method has been developed for simulating the multibody system with a large ratio of size and material modulus. The coupling is conducted through the contact force between SDEM particles and material points; both contact detection and the force calculation are unified under the contact scheme of the SDEM method. A serial of verification tests has been conducted using two different material constitutive models, linear elasticity, and Drucker-Prager

model. The conservation of energy, contact force, and mass transfer rate in granular flow has been investigated and analyzed with analytical solutions. Results have indicated that the conservation of energy is affected by the material properties but properly maintained in general. No extra energy was generated from the collision between material points and SDEM boundary, which guarantees the stability of the method. Contact forces, as the communicating value for the coupling, were correctly provided. Tests of granular flow have proved that our coupling scheme could effectively detect and handle the highly changeable contact relations between the MPM granular media and SDEM particles.

The motion of wooden blocks under the impact of the granular flow was conducted as a validation of the MPM-SDEM. Results have been compared with an existing MPM-DEM coupling method and experimental data. The variation of the rotational angle provided by MPM-SDEM has shown a better agreement with the experimental data. Results have also indicated that the MPM-SDEM overcomes the problems of the grid dependency and the oversimplification of rigid body motion in the existing method. Uniaxial compression tests for a granular matrix are performed as an application. It has further demonstrated that MPM-SDEM coupling method provides a scale-crossing solution for simulating the complex mechanical behavior of the granular matrix. Both continuous behavior of fines and discrete features of large particles can be well preserved in the simulation with optimal efficiency. Results have indicated that the fine percentage in a granular matrix imposes a major influence on its macroscale mechanical properties. In conclusion, the MPM-SDEM has its unique advantage for multibody interaction in solid dynamics that involves highly different sizes and material modulus. We anticipate it would make a good contribution to the study of geomechanics and CG.

ACKNOWLEDGMENTS

This research is financially supported by the Australia research council (ARC) linkage project "Performance of granular matrix under heavy haul cyclic loading" (LP160100280).

ORCID

Yupeng Jiang https://orcid.org/0000-0002-2040-2539

REFERENCES

1. Andrade JE, Avila CF, Hall SA, Lenoir N, Viggiani G. Multiscale modelling and characterization of granular matter from grain kinematics to continuum mechanics. *J Mech Phys Solid*. 2011;59:237-250.
2. Salot C, Gotteland P, Villard P. Influence of relative density on granular materials behavior: DEM simulations of triaxial tests. *Granul Matter*. 2009;11:221-236.
3. Kruyt NP. Micromechanical study of fabric evolution in quasi-static deformation of granular materials. *Mech Mater*. 2012;44:120-129.
4. Utili S, Zhao T, Houlsby GT. 3D DEM investigation of granular column collapse: evaluation of debris motion and its destructive power. *Engrg Geol*. 2015;186:3-16.
5. Dai Z, Huang Y, Cheng H, Xu Q. SPH model for fluid-structure interaction and its application to debris flow impact estimation. *Landslides*. 2017;14:917-928.
6. Teufelsauer H, Wang Y, Pudasaini SP, Borja RI, Wu W. DEM simulation of impact force exerted by granular flow on rigid structures. *Acta Geotech*. 2011;6:119-133.
7. Gao M, Tampubolon AP, Jiang C, Sifakis E. An adaptive generalized interpolation material point method for simulating elastoplastic materials. *ACM Trans Graph*. 2017;36(6):233:1-233:12.
8. Tampubolon AP, Gast T, Klár G, et al. Multi-species simulation of porous sand and water mixtures. *ACM Trans Graph*. 2017;36(4):105:2-105:11.
9. Huang H, Tutumluer E, Dombrow W. Laboratory characterization of fouled railroad ballast behavior. *Transp Res Rec*. 2009;2117:93-101.
10. Sol-Sánchez M, Thom NH, Moreno-Navarro F, Rubio-Gámez MC, Airey GD. A study into the use of crumb rubber in railway ballast. *Construct Build Mater*. 2015;75:19-24.
11. Kwan SHJ, Sze HYE, Lam C. Finite element analysis for rockfall and debris flow mitigation works. *Can Geotech J*. 2019;56:1225-1250.
12. Imseeh WH, Alshibli KA. 3D finite element modelling of force transmission and particle fracture of sand. *Comput Geotech*. 2018;94:184-195.
13. Lee NS, Bathe KJ. Error indicators and adaptive remeshing in large deformation finite element analysis. *Finite Elem Anal Des*. 1994;16:99-139.
14. Bardenhagen SG, Brackbill JU, Sulsky D. The material-point method for granular materials. *Comput Methods Appl Mech Eng*. 2000;187:529-541.
15. Gaume J, Gast T, Teran J, Herwijnen AV, Jiang C. Dynamic anticrack propagation in snow. *Nat Commun*. 2018;9:3047.
16. Wolper J, Fang Y, Li M, Lu J, Gao M, Jiang C. CD-MPM: continuum damage material point methods for dynamic fracture animation. *ACM Trans Graph*. 2019;119:1-15.
17. Bardenhagen SG, Guilkey JE, Roessig KM, Brackbill JU, Witzel WM, Foster JC. An improved contact algorithm for the material point method and application to stress propagation in granular material. *Comput Model Engrg Sci*. 2001;2(4):509-522.

18. Hu W, Chen Z. A multi-mesh MPM for simulating the meshing process of spur gears. *Comput Struct*. 2003;81:1991-2002.
19. Zhang HW, Wang KP, Chen Z. Material point method for dynamic analysis of saturated porous media under external contact/impact of solid bodies. *Comput Methods Appl Mech Eng*. 2009;198:1456-1472.
20. Guilkey JE, Harman T, Xia A, Kashiwa B, McMurtry P. An Eulerian-Lagrangian approach for large deformation fluid structure interaction problems, part 1: algorithm development. *WIT Trans Built Environ*. 2003;17:1-14.
21. Cundall PA, Strack ODL. A discrete numerical model for granular assemblies. *Geotechnique*. 1979;29(1):47-65.
22. Michael M, Vogel F, Peters B. DEM-FEM coupling simulations of the interactions between a tire tread and granular terrain. *Comput Methods Appl Mech Eng*. 2015;289:227-248.
23. Feng YT, Han K, Owen DRJ. Coupled lattice Boltzmann method and discrete element modelling of particle transport in turbulent fluid flows: computational issues. *Int J Numer Methods Eng*. 2007;72:1111-1134.
24. Zhong W, Yu A, Liu X, Tong Z, Zhang H. DEM/CFD-DEM modelling of non-spherical particulate systems: theoretical developments and applications. *Powder Tech*. 2016;302:108-152.
25. Liu C, Sun Q, Zhou GGD. Coupling of material point method and discrete element method for granular flows impacting simulations. *Int J Numer Methods Eng*. 2018;115:172-188.
26. Yue Y, Smith B, Chen PY, Chantharayukhonthorn M, Kamrin K, Grinspun E. Hybrid grains: adaptive coupling of discrete and continuum simulations of granular media. *ACM Trans Graph*. 2018;37(6):283:1-283:18.
27. Alonso-marroquín F, Wang Y. An efficient algorithm for granular dynamics simulations with complex-shaped objects. *Granul Matter*. 2009;11:317-329.
28. Jiang Y, Herrmann HJ, Alonso-Marroquin F. A boundary-spheropolygon element method for modelling sub-particle stress and particle breakage. *Comput Geotech*. 2019;103087:1-14.
29. Galindo-Torres SA. A coupled discrete element lattice Boltzmann method for the simulation of fluid-solid interaction with particles of general shapes. *Comput Method Appl Mech Eng*. 2013;265:107-119.
30. Sulsky D, Zhou SJ, Schreyer HL. Application of a particle-in-cell method to solid mechanics. *Comput Phys Commun*. 1995;87:236-252.
31. Jiang C, Schroeder C, Teran J, Stomakhin A, Selle A. The material point method for simulating continuum materials. *ACM SIGGRAPH 2016 Courses*. 2016;1-52.
32. Gan Y, Sun Z, Chen Z, Zhang X, Liu Y. Enhancement of the material point method using B-spline basis functions. *Int J Numer Methods Eng*. 2018;113:411-431.
33. Bardenhagen SG, Kober EM. The generalized interpolation material point method. *Comput Model Eng Sci*. 2004;5(6):477-496.
34. Jiang C, Schroeder C, Teran J. An angular momentum conserving affine-particle-in-cell method. *J Comput Phys*. 2017;338:137-164.
35. Bardenhagen SG. Energy conservation error in the material point method. *J Comp Phys*. 2002;180:383-403.
36. Evans MW, Harlow F. The particle-in-cell method for hydrodynamic calculation. *Los Alamos Sci Lab Report*. 1957.
37. Brackbill JU, Ruppel HM. FLIP: a method for adaptively zoned, particle-in-cell calculations of fluid flows in two dimensions. *J Comput Phys*. 1986;65:314-343.
38. Love E, Sulsky DL. An unconditionally stable energy-momentum consistent implementation of the material-point method. *Comput Methods Appl Mech Eng*. 2006;195:3903-3925.
39. Zhu Y, Bridson R. Animation sand as fluid. *ACM Trans Graph*. 2005;24(3):965-972.
40. Hammerquist CC, Nairn JA. Anew method for material point method particle updates that reduces noise and enhances stability. *Comput Methods Appl Mech Eng*. 2017;318:724-738.
41. Klár G, Gast T, Pradhana A, et al. Drucker-Prager elasto-plasticity for sand animation. *ACM Trans Graph*. 2016;35(4):103:1-103:12.
42. Molenkamp F. Limits to the Jaumann stress rate. *Int J Numer Anal Method Geomech*. 1986;10:151-176.
43. Courant R, Friedrichs K, Lewy H. On the partial difference equations of mathematical physics. *IBM J*. 1967;11(2):215-234.
44. Mankoc C, Janda A, Arévalo R, et al. The flow rate of granular materials through an orifice. *Granul Matter*. 2007;9(6):407-414.
45. Fu P, Dafalias YF. Study of anisotropic shear strength of granular materials using DEM simulation. *Int J Numer Anal Method Geomech*. 2011;35:1098-1126.

SUPPORTING INFORMATION

Additional supporting information may be found online in the Supporting Information section at the end of this article.

How to cite this article: Jiang Y, Li M, Jiang C, Alonso-Marroquin F. A hybrid material-point spheropolygon-element method for solid and granular material interaction. *Int J Numer Methods Eng*. 2020;1–27. https://doi.org/10.1002/nme.6345

APPENDIX A

The three-dimensional weighting functions for the GIMP is written as:

$$S_{Ip} = S_{xIp}(\mathbf{x}_p) \cdot S_{yIp}(\mathbf{x}_p) \cdot S_{zIp}(\mathbf{x}_p), \tag{A1}$$

where S_{iIp}, which is calculated based on the constant characteristic function and linear shape function, is defined as:

$$S_{iIp} = \begin{cases} 0, & x_{ip} - x_{iI} \le -(L + l_p) \\ [L + l_p + (x_{ip} - x_{iI})]^2/(4Ll_p), & -(L + l_p) < x_{ip} - x_{iI} \le -L + l_p \\ 1 + (x_{ip} - x_{iI})/L, & -L + l_p < x_{ip} - x_{iI} \le -l_p \\ 1 - [(x_{ip} - x_{iI})^2 + l_p^2]/(2Ll_p), & -l_p < x_{ip} - x_{iI} \le l_p \\ 1 + (x_{ip} - x_{iI})/L, & l_p < x_{ip} - x_{iI} \le L - l_p \\ [L + l_p - (x_{ip} - x_{iI})]^2/(4Ll_p), & L - l_p < x_{ip} - x_{iI} \le L + l_p \\ 0, & x_{ip} - x_{iI} > L + l_p \end{cases}, \tag{A2}$$

where L is the spacing of the background grid and l_p is the half size of the square influential area defined by the characteristic function χ_p. This weighting function is used for all the simulations of solid material.

Since the characteristic function is the Dirac delta function $\chi_p(\mathbf{x}) = \delta(\mathbf{x}_p)$, the three-dimensional weighting function for the APIC format is also the shape function which is using the quadratic kernel:

$$N_{Ip} = N_{xIp}(\mathbf{x}_p) \cdot N_{yIp}(\mathbf{x}_p) \cdot N_{zIp}(\mathbf{x}_p), \tag{A3}$$

where N_{iIp} is written as:

$$N_{iIp} = \begin{cases} (1/2)(|x_{ip} - x_{Ip}|/\mathrm{L})^3 - (|x_{ip} - x_{Ip}|/L)^2 + (2/3), & 0 \le |x_{ip} - x_{Ip}|/L < 1 \\ (1/6)(2 - |x_{ip} - x_{Ip}|/L)^3, & 1 \le |x_{ip} - x_{Ip}|/L < 2 \\ 0, & 2 \le |x_{ip} - x_{Ip}|/L \end{cases} \tag{A4}$$

.